Second-Surface Mirror Effects in Thin-Film Absorber Layers

José Dobarco-Otero

Thesis submitted to the Faculty of the

Virginia Polytechnic Institute and State University

in partial fulfillment of the requirements for the degree of

Master of Science

in

Mechanical Engineering

Dr. J.R. Mahan, Chairman

Dr. Brian Vick

Dr. Elaine Scott

September 2000

Blacksburg, Virginia

Second-Surface Mirror Effects in Thin-Film Absorber Layers

José Dobarco-Otero

Virginia Polytechnic Institute and State University, September 2000

Advisor: J. Robert Mahan

(ABSTRACT)

The Thermal Radiation Group at Virginia Polytechnic Institute and State University has been developing analytical and numerical heat transfer models for NASA's Langley Research Center for more than 25 years. Recent versions of these models are being used in the design of the next-generation thermal radiation detectors intended for Earth radiation budget campaigns. The current investigation presents three models for the absorption of electromagnetic radiation in thin films. The first assumes a surface heating boundary condition. The second model, derived from electromagnetic theory, is an analytical volumetric heat generation model. This model can be applied to a semi-infinite medium or to a thin-film absorber layers behaving as a second-surface mirror; that is, a semi-transparent coating deposited on top of a reflective surface. The third model is a statistical volumetric heat generation model that is derived using the Monte Carlo ray-trace (MCRT) method. These models are compared by using them to predict the transient temperature response of a generic thermal radiation detector. Results are presented for absorber layers in which the index of refraction is equal to the extinction coefficient. It was found that both of the volumetric heat generation models produce identical results. It was also found that the response of the detector due to shorter wavelengths deviates less from the surface absorption model than at longer wavelengths. A second-surface mirror reflection model for the absorber layer of the thermal radiation detector is also presented in this thesis.

Acknowledgments

First and foremost, I would like to thank my advisor, Dr. J. R. Mahan, for giving me the opportunity to do radiation heat transfer research. Without his advice, wisdom and support this thesis would not have been possible. His familiarity with my research topic was priceless.

I would like to express my gratitude to Dr. Elaine P. Scott and Dr. Brian Vick for serving on my advisory committee.

I am grateful to Mr. Robert B. Lee, III from NASA Langley Research Center for funding my research under NASA grant NAG-1-2128-SUPL3.

I am also indebted to the students of the Thermal Radiation Group for their helpful advice and friendship during this year: Edwin Ayala, Mamadou Barry, Hélène Brogniez, Bernardo Carnicero, Félix Nevárez, María Cristina Sánchez, María Santa María, Amie Smith, and Dwight E. Smith. A special thanks goes to Ira Sorensen for proofreading parts of my thesis and his tremendous help with Latex.

Last but certainly not least, I wish to thank my parents, José and María as well as my brother Paco for their love and unconditional support.

Contents

List of Figures

List of Tables

Nomenclature

Symbols:

A_c	Area (m^2)
c	Speed of light in medium (m/s)
D_{ij}	Distribution factor between surface elements i and j (-)
$\mathbf{E}$	Electric Field (V/m)
$\mathbf{H}$	Magnetic Intensity field (A/m)
i	Imaginary Number Operator, $\sqrt{-1}$
i_λ	Spectral Intensity ($W/m^2 \cdot sr \cdot \mu m$)
ℓ	constant length (μm)
n	Index of Refraction (-)
$\tilde{n}$	Complex Index of Refraction (-)
q	Heat Flux (W/m^2)
P	Period (s)
r	distance between plane area elements
r_e	Electrical Resistivity ($\Omega \cdot$m)
R	Resistance (Ω)
R_E	Radius of the Earth (m)

$\overline{R}$	Power Reflectance (-)
$\mathbf{S}$	Poynting Vector (W/m^2)
S_c	Solar Constant (W/m^2)
t	Time (s)
T	Temperature (K)
$\overline{T}$	Power Transmittance (-)
x	length (μm)
Z	Electrical Impedance/Resistance (Ω)

Greek:

$\overline{\alpha}$	Planetary Albedo (-)
ϕ	Phase Angle (rad)
γ	Permittivity of the Medium (C^2/N$\cdot$m^2)
Γ	Reflection Coefficient(-)
κ	Index of Extinction or Extinction Coefficient(-)
$\overline{\kappa}$	Band Averaged Spectral Coefficient (μm^{-1})
λ	Wavelength (μm)
σ	Stefan-Boltzmann Constant (W/m$^2\cdot$K^4)
μ	Permeability of the medium (N/A^2)
ν	Frequency (s^{-1})
τ	Transmission Coefficient ($-$)
$\overline{\tau}$	Transmissivity ($-$)
ω	Solid Angle (sr)

Subscripts:

0	Quantity in Vacuum
in	Incident
r	Reflected
t	Transmitted
y	y-polarized

Supercripts and Overbars:

$*$	Complex Conjugate
$'$	Real Component
$''$	Imaginary Component
$\tilde{}$	Complex Quantity
(*bold*)	Vector

Constants:

c_0	Speed of Light in Vacuum, 2.997925×10^8 m/s
c_1	Blackbody Intensity Constant, 1.191×10^8 W$\cdot\mu$m^4/m$^2\cdot$sr
R_E	Radius of the Earth, 6.375×10^6 m
c_2	Blackbody Intensity Constant, 1.439×10^4 μm$\cdot$K

γ_0	Permittivity of the Medium, 8.854×10^{8} $C^2/N\cdot m^2$
σ	Stefan-Boltzmann Constant, 5.668×10^{8} $W/m^2\cdot K^4$
μ_0	Permeability of Free Space, $4\pi\times10^{-8}$ N/A^2

Chapter 1

Introduction

An important class of thermal radiation detectors operates on the bolometer principle. A generic thermistor bolometer concept is shown in Figure 1.1. It consists of a thermistor coated with an absorber layer and in thermal contact with a heat sink through a thermal impedance. In order to attain a fast response, its thermal mass must be small. This implies a thin absorber layer, which brings up an important question: "Can an absorber layer 10 μm thick be an effective absorber of 50 μm radiation?" This thesis attempts to provide some insight to this question, posed by a senior NASA scientist some years ago.

1.1 Description of the Thermal Radiation Detector

The thermal radiation detector modeled in this thesis is a thermopile bolometer. It consists of six parallel layers of different materials and a heat sink. Figure 1.2 shows the configuration of the detector. A 1-μm thick platinum layer is deposited on top of an aluminum-nitride substrate. A 1-μm thick zinc-antimonide layer is deposited on top of the platinum layer. This

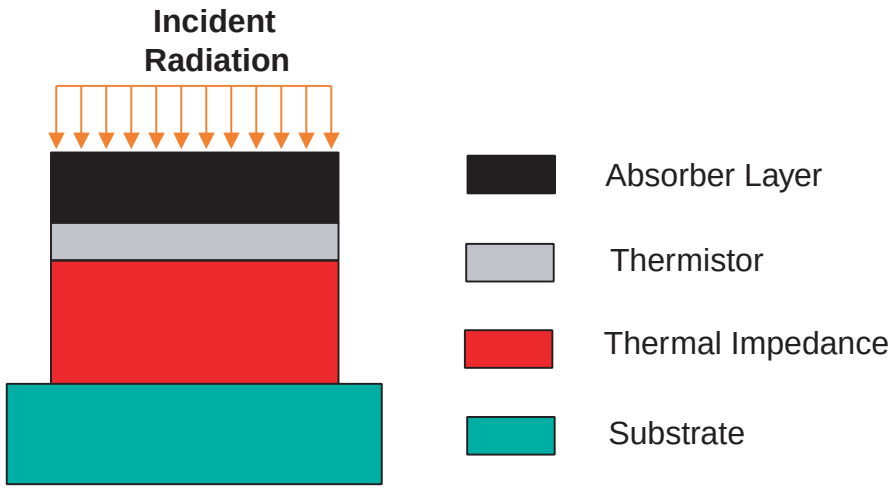

Figure 1.1: A generic bolometer thermal radiation detector.

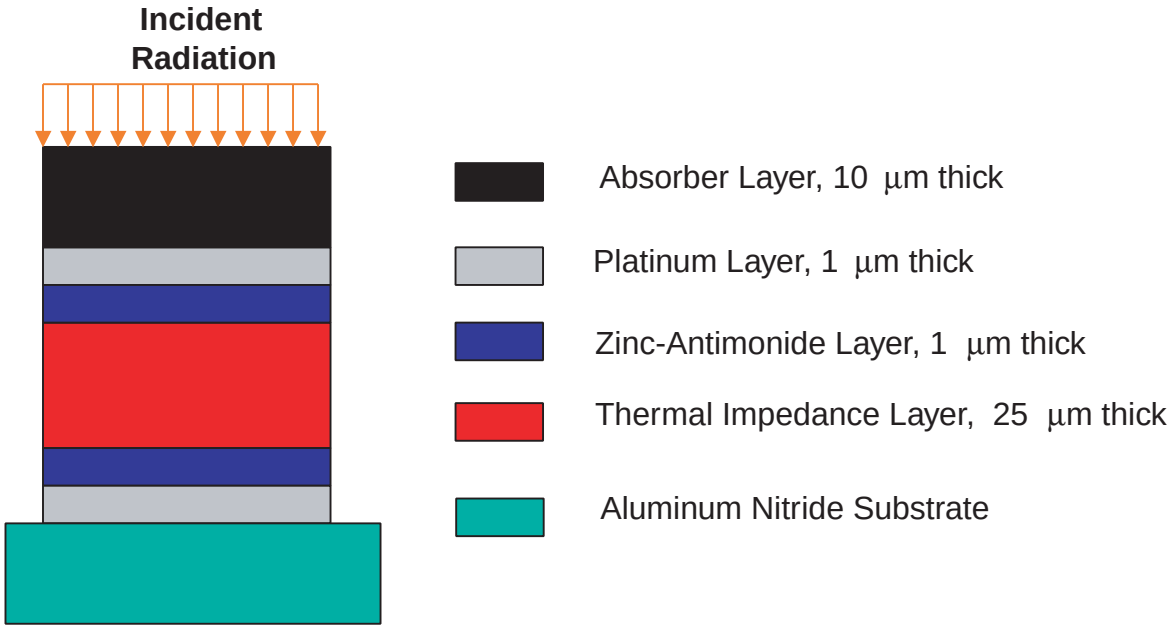

Figure 1.2: Baseline model of the thermal radiation detector investigated in this thesis.

platinum/zinc-antimonide interface acts as the reference junction of the detector. Next, a 25-μm thick layer of a good thermal insulator such as parylene, which acts as the thermal impedance layer, is bonded on top of the zinc-antimonide layer. Additional 1-μm thick platinum and zinc-antimonide layers are added to form the active junction of the detector. Finally, a 10-μm-thick absorber layer typically composed of Chemglaze Z-306 or equivalent, is provided to increase the broadband absorption of incident radiation. The thermophysical properties of the materials used in the baseline thermal radiation detector model are given in Table 1.1.

A version of the detector described above was conceived for use in the Geosynchronous Earth Radiation Budget (GERB) instrument, an European initiative to measure broadband radiances leaving the Earth. The shortwave band was to be sensitive from 0.32 to 4 μm, and the longwave band from 4 to 30 μm. The total radiation would then be the sum of the combined shortwave and longwave responses. Shortwave radiation originates from the sun and longwave radiation is emitted by the Earth. More information on the proposed instrument is given by Weckmann [1997], Sánchez [1998], and Sorensen [1998].

1.2 Motivation for Research

The Thermal Radiation Group (TRG), under the leadership of Dr. J. Robert Mahan in the Department of Mechanical Engineering at Virginia Polytechnic Institute and State University, has been working for the past several years on the development of the next generation of thermal radiation detectors for the observation of the Earth's radiation budget from orbiting platforms. In the recent past, the members of the TRG have modeled various aspects of this detector [Weckmann, 1997; Sorensen, 1998; Sánchez, 1998; Barry, 1999] assuming a radiant

Table 1.1: Nominal material properties used in the baseline detector model [Weckmann, 1997].

Material	Mass Density (kg/m^3)	Specific Heat (J/kg·K)	Conductivity (W/m·K)
Platinum	21450	133	71.6
Zinc-Antimonide	6880	200	60
Aluminum Nitride	3260	800	165
Thermal Impedance	1289	712	0.084
Absorber Layer	1400	669	0.209

heat flux incident to the surface of the absorber layer, as illustrated in Figure 1.2. Instead of modeling the incident radiation as a surface phenomenon, in this thesis the incident radiation is modeled as a nonuniform internal heat generation within the absorber layer. This is because a significant amount of the incident radiation is at wavelengths equal to or longer than the thickness of the absorber layer. Figure 1.4 illustrates how incident radiation is attenuated in the absorber layer. The variables denoting the envelope will be explained in more detail in the next chapters. In this more realistic view of absorption, the upper surface of the absorber is assumed to be insulated as is shown in Figure 1.3. The other boundary condition at the aluminum-nitride substrate is modeled as a constant temperature surface, as in the original model of Figure 1.2.

The work described in this thesis constitutes the initial step in a methodology for the estimation of electrical and thermal properties of candidate detector materials. These include the electrical resistance, the complex index of refraction and perhaps even more exotic properties such as the permittivity for diamagnetic media. Standard techniques, such as evolutionary

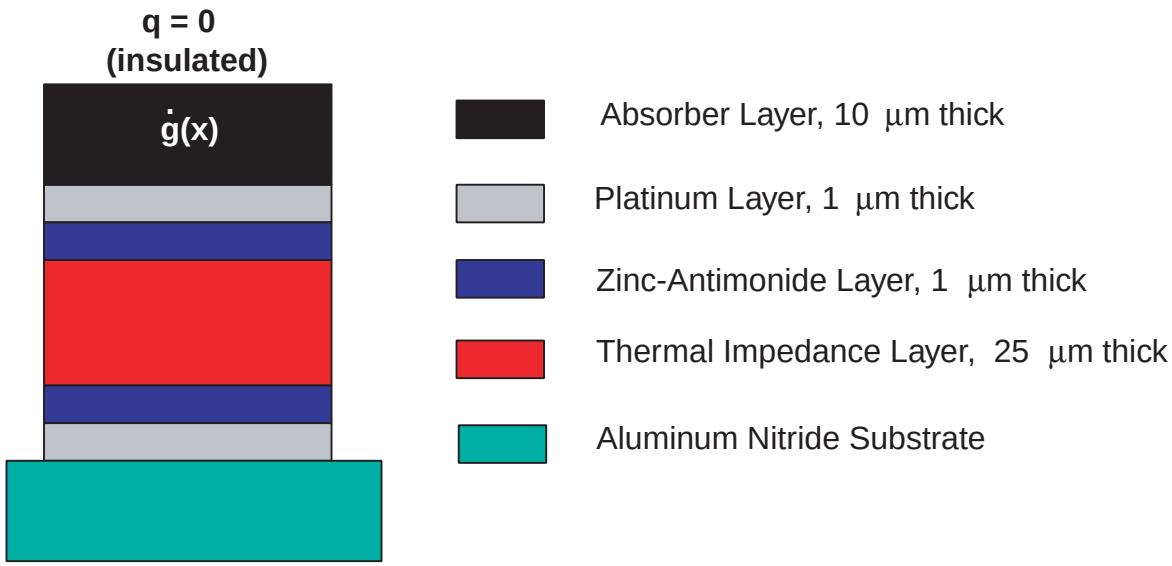

Figure 1.3: Model of the thermal radiation detector used in this thesis.

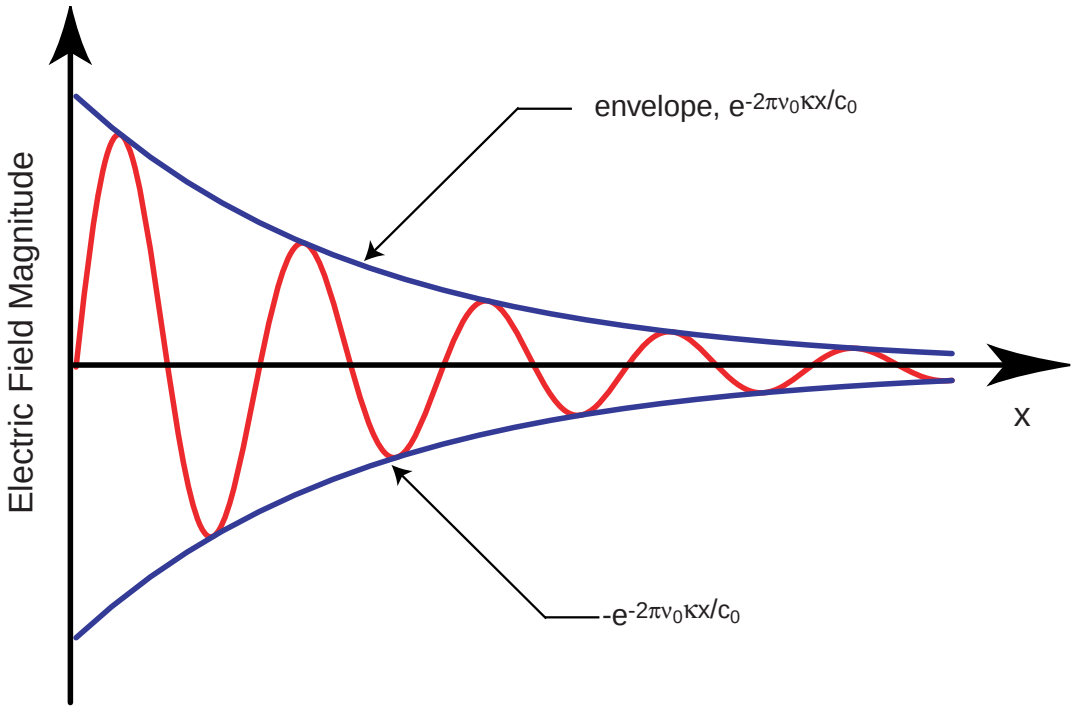

Figure 1.4: Extinction of electromagnetic wave in an absorbing medium.

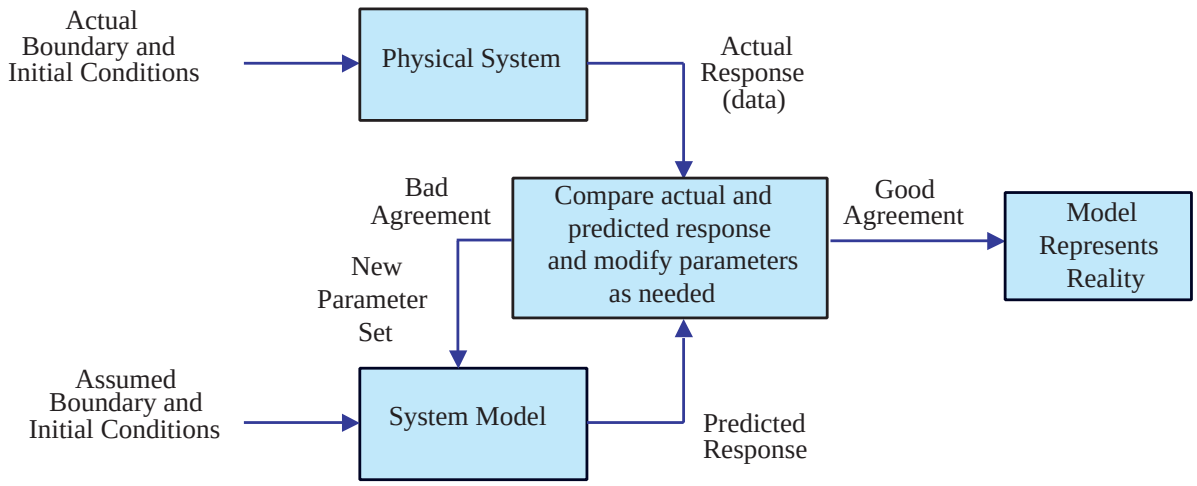

Figure 1.5: Logic flow chart of a generic parameter estimation methodology.

algorithms (EAs), may be used to estimate the values of parameters of a model by systematically varying these values in such a way as to minimize the difference between the predicted and observed response of the modeled system to external stimuli. The logic flow chart of a typical parameter estimation process is presented in Figure 1.5. In a parameter estimation process we have a system having certain physical properties such as the complex index of refraction or the electrical resistivity. This system also has boundary conditions such as the distribution of the incident radiation, as well as initial conditions, such as the initial temperature distribution. The boundary and initial conditions acting on a system give rise to the response of the system, which in this case could be the temperature rise at key locations within the physical system. To retrieve properties we need a model that takes into consideration the relevant physics of the system. Now assuming reasonable boundary and initial conditions we can change the properties of the model until the response of the model agrees with the measured response.

The specific procedure for estimating the properties of the absorber layer is illustrated by

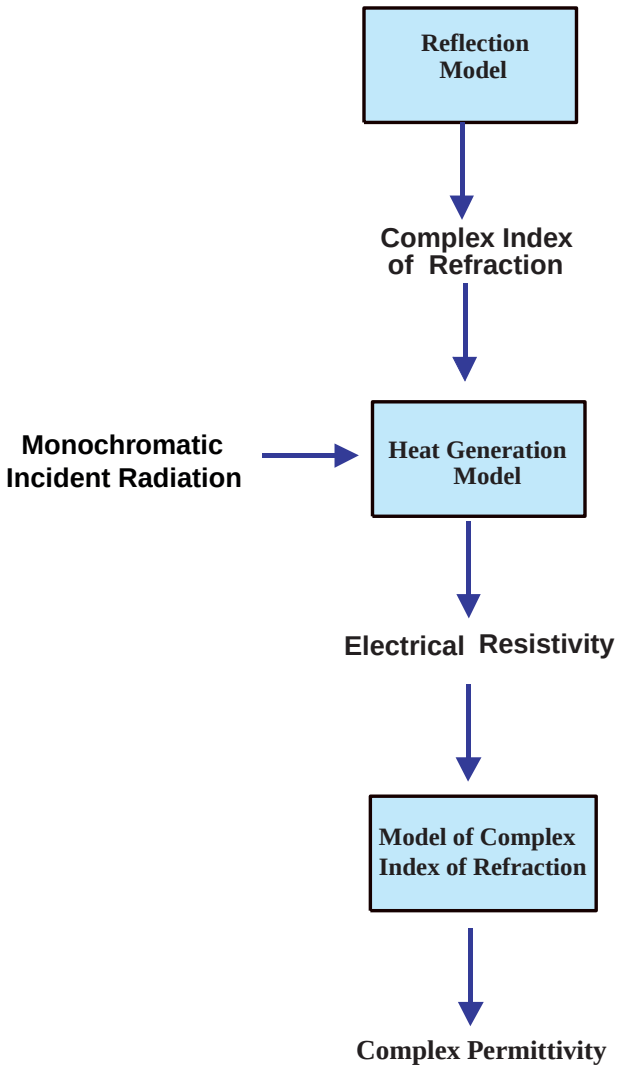

Figure 1.6: Logic flow chart for analytical estimation of absorber properties.

the logic flow chart in Figure 1.6. This is a three-step process. First, the complex index of refraction is predicted by applying the parameter estimation methodology depicted in Figure 1.5 to the absorber reflection model. The predicted complex index of refraction should reproduce the measured reflection data when it is entered in the reflection model. Next, the electrical resistivity is estimated by carrying out numerical experiments with the heat generation model at a given wavelength. The correct value of the electrical resistivity is obtained when the heat generation in the absorber is equal to the amount of energy absorbed in the layer due to an incident electromagnetic wave. Since electrical resistivity is not dependent on wavelength, the electrical resistivity can be used at other wavelengths to validate the heat generation model. Finally, knowing the electrical resistivity of the absorber layer, the complex permittivity can be found by using well-known models relating the complex index of refraction to the transmission and absorption of electromagnetic energy within the medium.

1.3 Thesis Objectives

The goals of the current investigation are:

1. Develop an analytical model derived from electromagnetic theory in which absorbed radiation is treated as a volumetric heat generation.

2. Validate aspects of this model using the Monte Carlo ray-trace method.

3. Compare the heat generation conduction models with the existing surface absorption model by predicting the transient temperature response of the thermal radiation detector.

4. Develop an analytical reflection model that takes into consideration the thin-film nature of the absorber layer.

1.4 Thesis Preview

The remaining chapters of this thesis are organized in the following manner. Chapter 2 reviews some useful fundamental concepts from radiation heat transfer and optics. In Chapter 3, the heat generation and reflection model for the absorber layer is derived from electromagnetic theory and Chapter 4 introduces the Monte Carlo ray-trace (MCRT) method applied to participating media. Finally, Chapter 5 presents the results of the theory developed in the previous two chapters, and Chapter 6 summarizes and draws conclusions from the results of Chapter 5 and identifies areas for further research.

Chapter 2

Some Fundamental Ideas from Radiation Heat Transfer and Optics

This chapter reviews five concepts that are used in the subsequent chapters: the blackbody, the solid angle, the Earth radiation budget, the electrical resistivity, and the complex index of refraction. Section 2.1 briefly reviews the blackbody model of radiation heat transfer, which is subsequently used to model radiation emitted by the Earth. Section 2.2 introduces the reader to the solid angle, another important concept in radiation heat transfer. Next, Section 2.3 uses background introduced in the Sections 2.1 and 2.2 to derive a simple model for relevant aspects of the Earth radiation budget. Following this, Section 2.4 introduces the electrical resistivity, an important parameter in the heat generation model referred in Chapter 1. Finally, Section 2.5 introduces the index of refraction from Maxwell's equations which, like the electrical resistivity, is an important parameter in the heat generation model developed in Chapter 3.

2.1 The Blackbody

Prevost's law states that any body at a temperature greater than absolute zero emits radiation. All bodies that emit radiation according the Stefan-Boltzmann law are by definition blackbodies. The Stefan-Boltzmann law is

$$q_e = \sigma T^4 \ , \tag{2.1}$$

where σ is the Stefan-Boltzmann constant (5.668×10^{-8} W/m^2·K^4), q_e is the emitted heat flux in W/m^2, and T is the absolute temperature in K.

The Stefan-Boltzmann law does not describe the distribution with wavelength of the emitted radiation. This relationship is described by the Planck blackbody radiation distribution function,

$$i_{BB,\lambda}(\lambda, T) = \frac{c_1}{\lambda^5[e^{c_2/(\lambda T)} - 1]} \ , \tag{2.2}$$

where λ is the wavelength (μm), $i_{BB,\lambda}(\lambda, T)$ is the spectral blackbody intensity (W/m^2 · μm·sr), and c_1 and c_2 are constants equal to 1.191×10^8 W·μm^4/m^2·sr and 1.439×10^4 μm·K, respectively.

The Planck function multiplied by π is the spectral hemispherical emissive power. When spectral hemispherical emissive power is integrated over all wavelengths, the corresponding result is the Stefan-Boltzmann law; that is,

$$q = \int_0^\infty \frac{\pi c_1}{\lambda^5[e^{c_2/(\lambda T)} - 1]} d\lambda = \sigma T^4 \ . \tag{2.3}$$

Before Planck published the correct expression, in 1901, for the blackbody radiation distribution function, Wien proposed the expression

$$i_{Wien,\lambda}(\lambda, T) = \frac{c_1}{\lambda^5 e^{c_2/(\lambda T)}} \ . \tag{2.4}$$

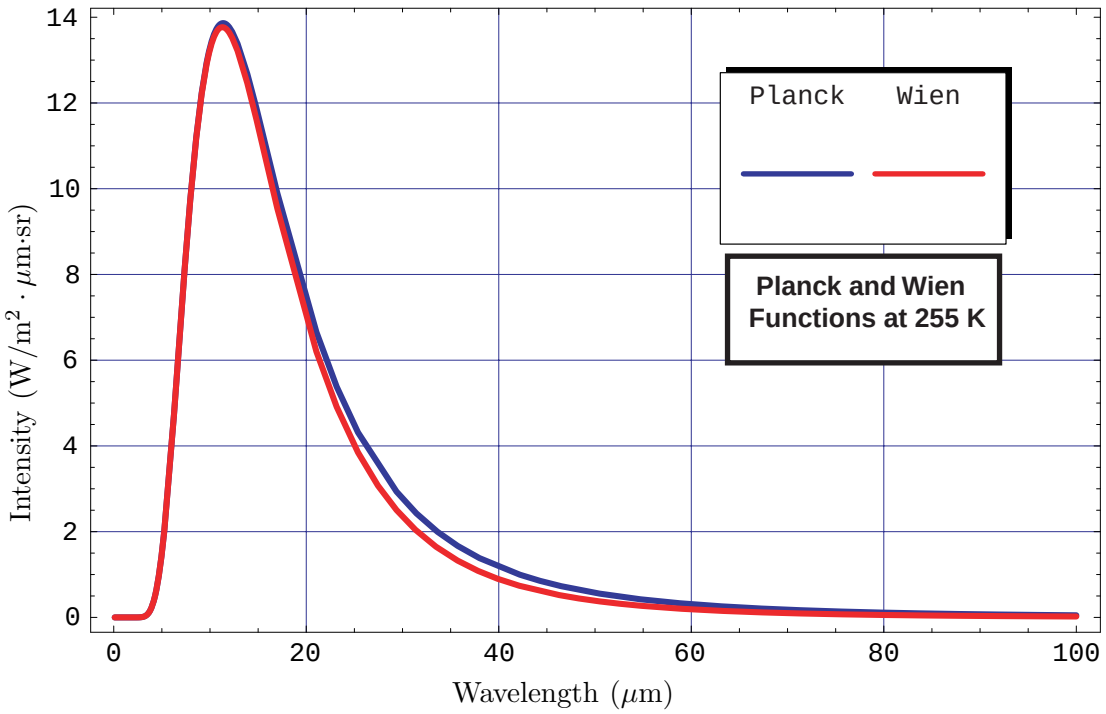

Figure 2.1: Planck and Wien blackbody functions

The difference between the Planck blackbody radiation distribution function and Wien's expression becomes apparent as the temperature approaches infinity: Planck's function approaches zero as the wavelength approaches infinity, while Wien's function approaches a finite value, c_1/λ^5. It is interesting to point out that a total energy difference of only about eight percent exists between the Planck and the Wien blackbody radiation distribution functions for a blackbody at 255 K. The error between Planck's function and Wien's function varies widely in different wavelength intervals; for example in the wavelength interval between 10 and 20 μm the error is less than three percent, while the error between 50 and 75 μm is about sixty-two percent. The distribution of this difference with wavelength can be seen, though in a misleading manner, in Figure 2.1.

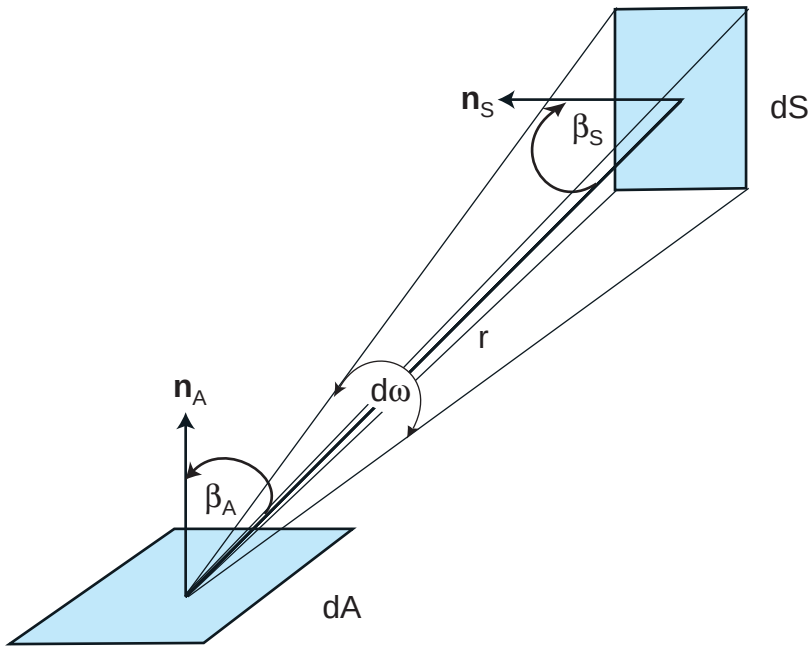

Figure 2.2: Definition of the differential solid angle [Mahan, 2000]

2.2 The Solid Angle

The differential solid angle dω subtended by a plane area element dS at a plane area element dA is defined as

$$d\omega = \frac{dS \cos \beta_s}{r^2} \ , \tag{2.5}$$

where r is the distance between the two plane area elements, β_s is the angle between the unit normal vector of plane area dS and the unit vector in the direction of the line of length r. This is shown by Figure 2.2. The solid angle is a dimensionless ratio of area over length squared and has the units of steradians (sr).

If the differential solid angle is subtended by a differential spherical sector, the $\cos \beta_s = 1$. Therefore, the projected area of the differential spherical sector viewed from the center of

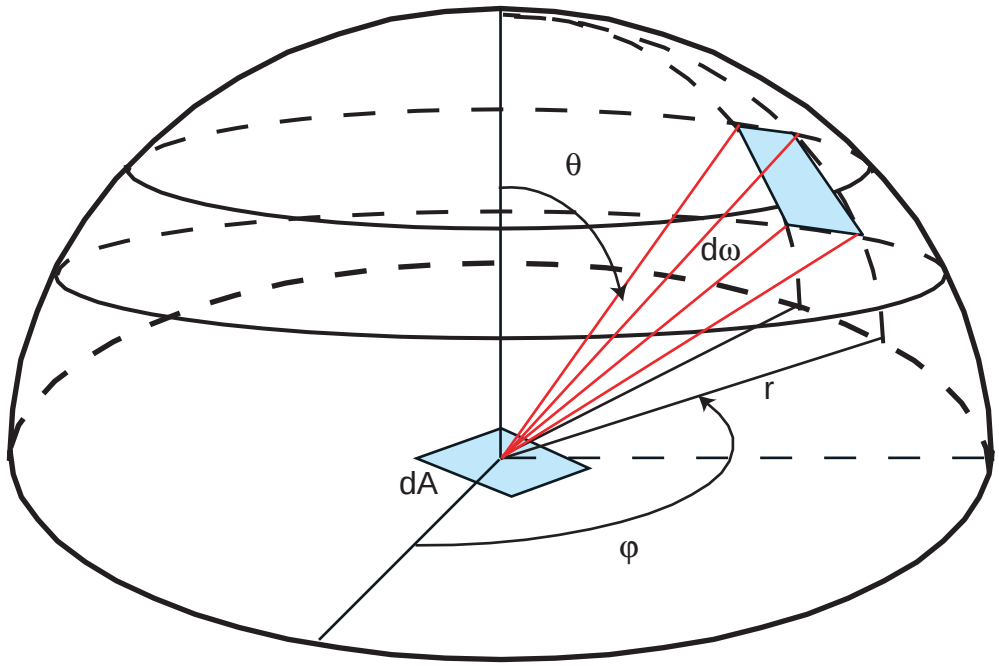

Figure 2.3: Differential solid angle subtended by a spherical sector at the center of a sphere.

the sphere is

$$dS = (r \sin\theta d\phi)(r d\theta) = r^2 \sin\theta d\theta d\phi \ . \tag{2.6}$$

Then from the definition of the solid angle, Equation 2.5, we have

$$d\omega = \sin\theta d\theta d\phi \ . \tag{2.7}$$

Thermal radiation detectors similar to those described in Chapter 1 are presently on board low-Earth-orbit satellites, such as the Tropical Rainfall Measuring Mission [NASA, 2000] and Terra [Bordi et al., 1997], that orbit the Earth at an altitude of 705 km, in the case of the latter. From the geometry in Figure 2.4, the solid angle subtended by the Earth as viewed

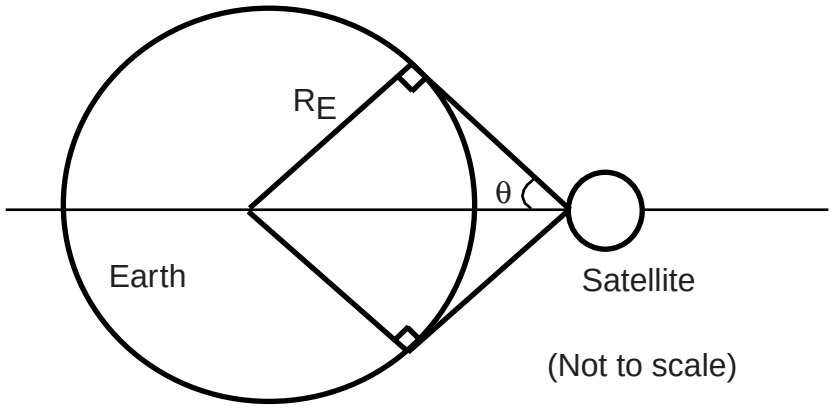

Figure 2.4: Geometry between the Earth and the Terra satellite

by the satellite is calculated to be 2.676 sr. This value is used in subsequent analysis in this thesis. The importance of the solid angle will be seen in the following chapters, since the solid angle determines how much of the radiation emitted by the Earth reaches the satellite.

2.3 The Earth Radiation Budget

If the sun is modeled as a sphere with an effective blackbody temperature of 5785 K, a theoretical solar constant of S_c=1382 W/m^2 is obtained by integrating the Planck function over all wavelengths and using a solid angle of 2×10^{-5} sr. Note that this is not σT_{SUN}^4 because of the distance from the sun the solid angle is not π. The theoretical value is in adequate agreement with the measured value of S_c=1366 W/m^2 [Lee et al., 1995]. Therefore, we can write a simple energy balance on the Earth to obtain the effective blackbody temperature of the Earth-atmosphere system. This may be written symbolically as

$$\frac{S_c}{4}(1-\overline{\alpha}) = \sigma T_{EARTH}^4 \ , \tag{2.8}$$

where $\overline{\alpha}$ is planetary albedo. The planetary albedo, $\overline{\alpha}$, is the fraction of incident solar

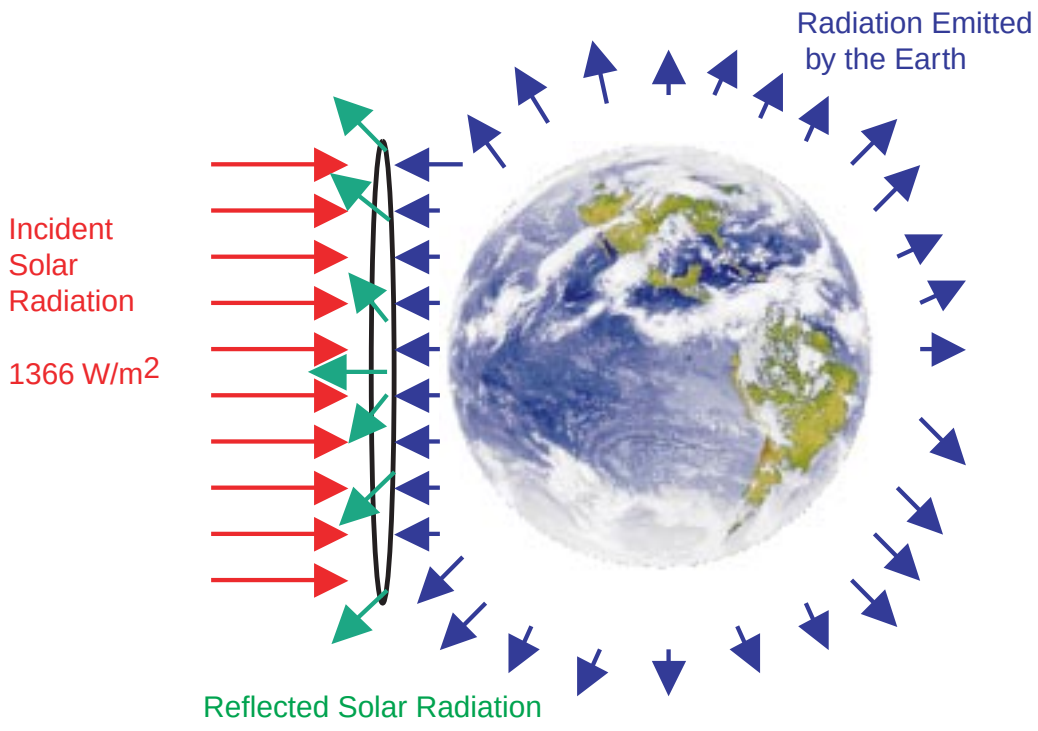

Figure 2.5: The Earth radiation budget.

irradiance reflected by the Earth. Equation 2.8 states that the incident solar radiation absorbed by the Earth must be balanced by emission. Satellite measurements in the past have indicated that the planetary albedo is 0.30 ± 0.03 [Ramanathan et al., 1989]. In Equation 2.8 the solar constant is divided by 4 to take into consideration the ratio of Earth's surface area, $4\pi R_E^2$ to the Earth's disk area, πR_E^2. Equation 2.8, with $\overline{\alpha} = 0.30$, gives an effective blackbody temperature of the Earth of 255 K. Figure 2.5 illustrates the Earth energy balance.

2.4 Electrical Resistivity

The electrical resistivity, r_e, is a material property independent of geometry. For a specimen of length ℓ and uniform cross-sectional area A_c, it is related by electrical resistance, R, by

$$r_e = \frac{RA}{\ell} \ , \tag{2.9}$$

where ℓ is the distance between the two points at which the voltage is known and A is the cross-sectional area normal to the direction of the current flow. Figure 2.6 shows a schematic diagram of an apparatus used to measure electrical resistivity. A battery provides a constant voltage, E_V. A variable resistor, R_V, is used to regulate the current in the circuit. The current, I, is measured with an ammeter. Using a voltmeter, the voltage drop is measured across the specimen. Now Ohm's law, R = V/I may be used to find the resistance of the specimen, after which Equation 2.9 can be used to compute the resistivity of the material.

The electrical resistivity of Chemglaze, which is basically composed of carbon-black particles suspended in a binder, is currently unknown. The electrical resistivity of carbon black itself is very much dependent on the way carbon black was made [Blythe, 1979]. Blythe [1979] also notes that the electrical conductivity of carbon-black composite depends very much on the

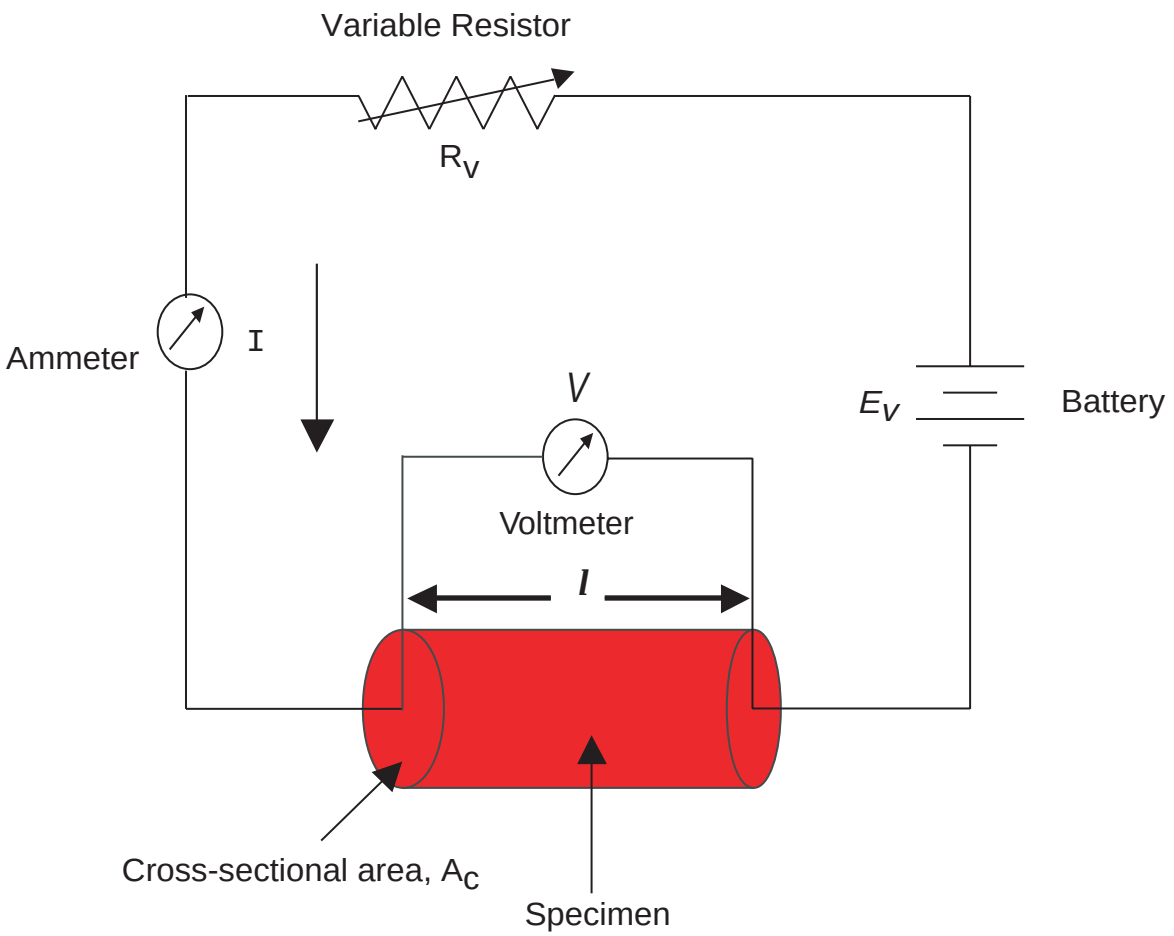

Figure 2.6: Schematic diagram of an experimental arrangement used to measure electrical resistivity.

concentration of carbon black, as illustrated on Figure 2.7. Typical values for the electrical resistivity of a carbon-black filled conductive paint are shown in Table 5.2.

Table 2.1: Electrical resistivity of carbon-black-filled paint [Calahorra, 1988].

Volume Concentration (Percent)	Electrical Resistivity (Ω·cm)
15.4	33.3
27.4	2.6
29.0	4.15
30.1	3.5
31.25	1.64
34.6	12.0
37.7	25.4

2.5 Complex Index of Refraction

Maxwell's equations describe the propagation of electromagnetic energy through a medium. Two of the four Maxwell's equations for an isotropic medium are

$$\nabla \times \tilde{\mathbf{H}} = \tilde{\gamma}\frac{\partial \tilde{\mathbf{E}}}{\partial t} + \frac{\tilde{\mathbf{E}}}{r_e} \tag{2.10}$$

and

$$\nabla \times \tilde{\mathbf{E}} = \tilde{\mu}\frac{\partial \tilde{\mathbf{H}}}{\partial t} \ . \tag{2.11}$$

where $\tilde{\gamma}$ is the complex permittivity, $\tilde{\mu}$ is the complex permeability, $\tilde{\mathbf{E}}$ is the complex instantaneous electric field in V/m, and $\tilde{\mathbf{H}}$ is the complex instantaneous magnetic field intensity in A/m. In addition to being complex, note that $\tilde{\mathbf{E}}$ and $\tilde{\mathbf{H}}$ are also vector quantities.

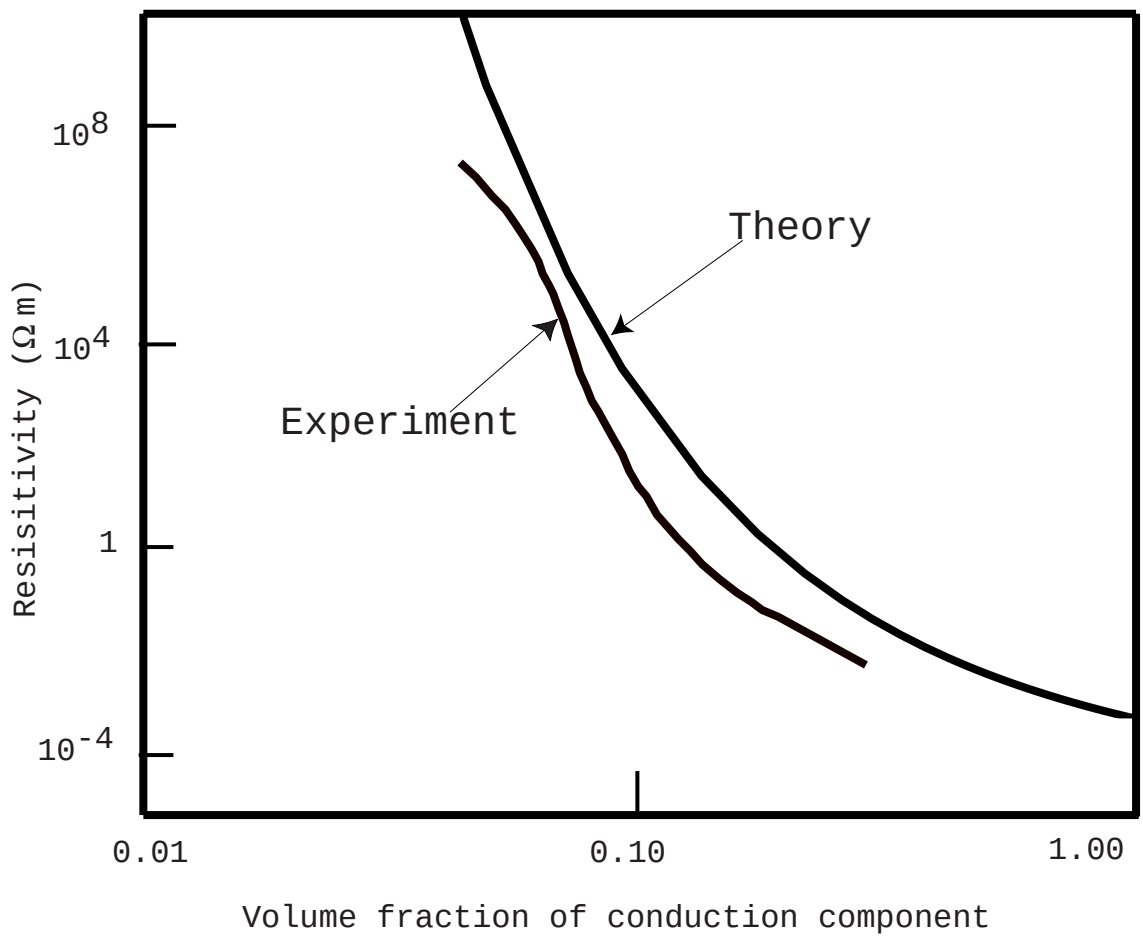

Figure 2.7: Comparison of experimental and theoretical dependance of resistivity on carbon-black content in a polyethylene composite [Blythe, 1979].

Equations 2.10 and 2.11 can be expressed in orthogonal x, y, z, and t coordinates to yield two sets of three equations. Consider a y-polarized plane wave propagating through a homogenous medium in the x-direction. In this case, all quantities are constant in the yz-plane; that is, $\partial/\partial y = \partial/\partial z = 0$.

Then from Equation 2.10 we obtain

$$-\frac{\partial \tilde{H}_z}{\partial x} = \tilde{\gamma}\frac{\partial \tilde{E}_y}{\partial t} + \frac{\tilde{E}_y}{r_e} \tag{2.12}$$

and from Equation 2.11 we obtain

$$\frac{1}{\tilde{\mu}}\frac{\partial \tilde{E}_y}{\partial x} = -\frac{\partial \tilde{H}_z}{\partial t} \ . \tag{2.13}$$

Eliminating the magnetic field strength, $\tilde{H}_z$ between these two equations yields

$$\tilde{\mu}\tilde{\gamma}\frac{\partial^2 \tilde{E}_y}{\partial t^2} = \frac{\partial^2 \tilde{E}_y}{\partial x^2} - \frac{\tilde{\mu}}{r_e}\frac{\partial \tilde{E}_y}{\partial t} \ . \tag{2.14}$$

The permeability and permittivity are complex quantities; that is $\tilde{\mu} = \mu' + i\mu''$ and $\tilde{\gamma} = \gamma' + i\gamma''$, respectively, where $i = \sqrt{-1}$ is the imaginary operator. Two expression for the complex index of refraction, $n - i\kappa$, can be obtained from Equation 2.14 by equating the real and imaginary terms. When this is done these results

$$n^2 - \kappa^2 = c_0^2(\mu'\gamma' - \mu''\gamma'') - \frac{\mu''\lambda_0 c_0}{2\pi r_e} \tag{2.15}$$

and

$$n\kappa = \frac{(\mu''\gamma' - \mu'\gamma'')c_0}{2} + \frac{\mu'\lambda_0 c_0}{4\pi r_e} \ , \tag{2.16}$$

where λ_0 is the wavelength in vacuum in meters and c_0 is the speed of light in a vacuum (2.997×10^8 m/s).

Solving Equations 2.15 and 2.16 for κ and n yields

$$n^2 = \frac{c_0}{4\pi r_e}(-\lambda_0\mu'' + 2c_0\pi r_e(-\gamma''\mu'' + \gamma'\mu') + [4c_0\pi r_e\gamma''\lambda_0(\mu''^2 - \mu'^2) + \lambda_0^2(\mu''^2 + \mu'^2)$$
$$+ 4c_0^2\pi^2 r_e^2\{-4\gamma''\gamma'\mu'\mu'' + \gamma''^2\left(\mu''^2 + \mu'^2\right) + \gamma'^2(\mu''^2 + \mu'^2)\}]^{1/2}(\ ) \ . \quad (2.17)$$

and

$$\kappa^2 = \frac{c_0}{4\pi r_e}(\lambda_0\mu'' + 2c_0\pi r_e(\gamma''\mu'' - \gamma'\mu') + [4c_0\pi r_e\gamma''\lambda_0(\mu''^2 - \mu'^2) + \lambda_0^2(\mu''^2 + \mu'^2)$$
$$+ 4c_0^2\pi^2 r_e^2\{-4\gamma''\gamma'\mu'\mu'' + \gamma''^2\left(\mu''^2 + \mu'^2\right) + \gamma'^2(\mu''^2 + \mu'^2)\}]^{1/2}\ ) \ . \quad (2.18)$$

The real part of the complex index of refraction, n, is the ratio of the speed of light in vacuum to that of the medium; that is $n \equiv c/c_0$. The physical meaning of the index of extinction, κ, is illustrated Figure 1.4. The index of extinction, or extinction coefficient, determines the distance the electromagnetic wave will travel in a medium before being absorbed.

If $\tilde{\gamma}$ and $\tilde{\mu}$ are real, then Equations 2.18 and 2.17 reduce to

$$n^2 = \frac{\mu'\gamma' c_0^2}{2}\left[1 + \sqrt{1 + \left(\frac{\lambda_0}{2\pi r_e\gamma'}\right)^2}\right] \quad (2.19)$$

and

$$\kappa^2 = \frac{\mu'\gamma' c_0^2}{2}\left[-1 + \sqrt{1 + (\frac{\lambda_0}{2\pi r_e\gamma'})^2}\right] \ . \quad (2.20)$$

Equations 2.19 and 2.20 may be found in radiation heat transfer textbooks, such as the one by Seigel and Howell [1992].

For diamagnetic media such as the absorber layer under consideration here Cheng [1992] notes that $\mu \cong \mu_0$. Cheng [1992] also points out that for low-loss dielectrics such as Chemglaze, $\gamma'' << \gamma'$, but still γ'' cannot be neglected because if γ'' were to be completely neglected the material would be a perfect dielectric.

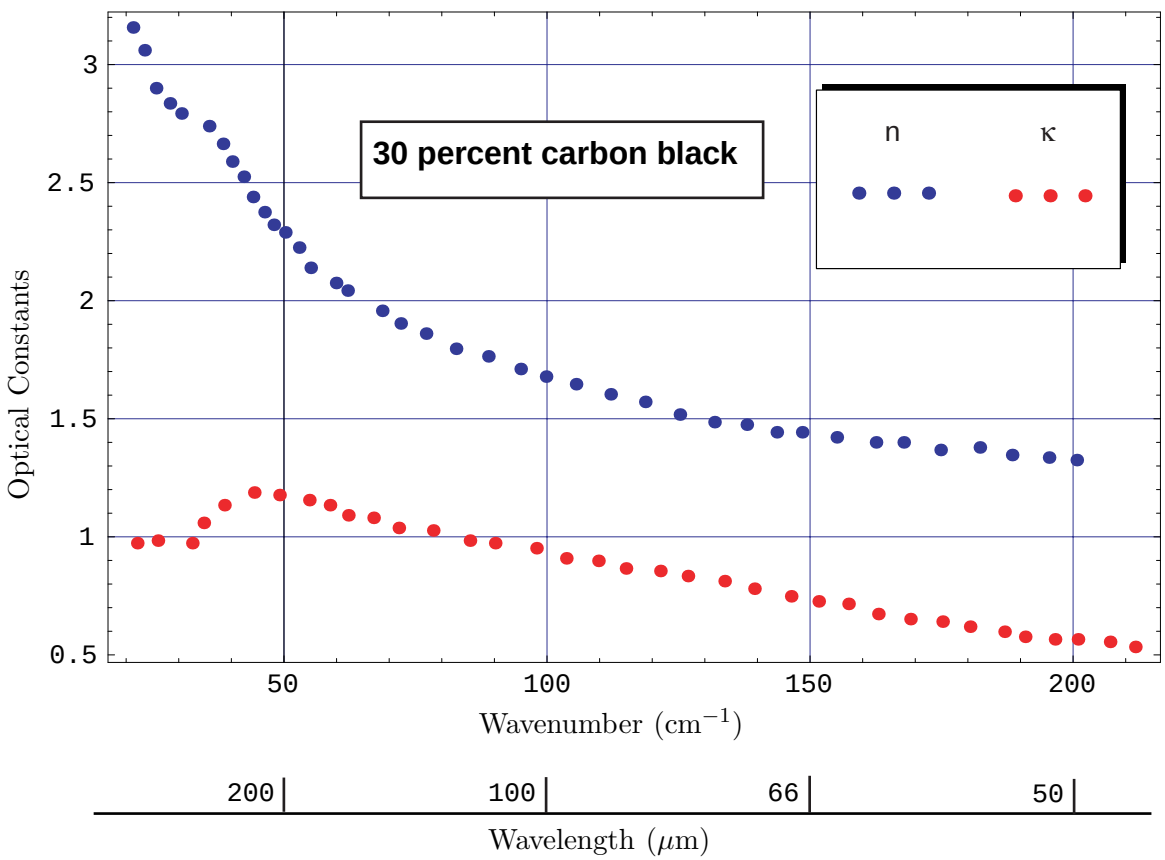

Figure 2.8: Optical constants for a carbon-black-loaded binder [Grammer et al., 1980].

Table 2.2: Comparison of measured optical constants with electromagnetic theory predictions [Seigel and Howell, 1992].

Metal	Wavelength λ_0, (μm)	Electrical Resistivity r_e, (Ω-cm)	Refractive Index n	Extinction Coefficient κ	Hagen-Rubens $n = \kappa$
Aluminum	12	2.82×10^{-6}	33.6	76.4	113
Copper	5.50	1.72×10^{-6}	3.16	28.4	98
Gold	5.00	2.44×10^{-6}	1.81	32.8	78
Platinum	5.00	10×10^{-6}	11.5	15.7	39
Silver	4.50	1.63×10^{-6}	4.49	33.3	91

At the turn of the century, Hagen and Rubens [1900] proposed that for metals (electrical conductors, small r_e) at sufficiently long wavelengths ($\lambda \geq 5$ μm),

$$\kappa \cong n \cong \sqrt{\frac{\lambda_0 \mu_0 c_0}{4\pi r_e}} \ . \tag{2.21}$$

The Hagen-Rubens theory can be used to estimate optical constants without knowing the permeability and the permittivity of the medium.

Properties such as the permeability of the medium, $\tilde{\mu}$, and the permittivity of the medium, $\tilde{\gamma}$, for commercial coatings such as Chemglaze have not been reported in the literature. Other investigators, such as Smith and Howitt [1986] use data for a carbon-black-loaded binder to approximate the optical constants of Chemglaze. For example, data of this type from Grammer et al. [1980] are shown in Figure 2.8. Later in this thesis the Hagen-Rubens approximation, Equation 2.21 is used to approximate κ and n for these materials. It is noted that the variation from this approximation so obvious in Figure 2.8 is no worse than for common metals as seen in Table 2.2. However, as it can be seen from Table 2.3, the Hagen-

Table 2.3: Comparison of measured and predicted emissivities by the Hagen-Rubens theory [Seigel and Howell, 1992].

Metal	Wavelength λ_0, (μm)	Electrical Resistivity r_e, (Ω-cm)	Measured Spectral Normal Emissivity	Predicted Spectral Normal Emissivity
Aluminum	12	2.82×10^{-6}	0.02	0.018
Copper	5.50	1.72×10^{-6}	0.012	0.020
Gold	5.00	2.44×10^{-6}	0.031	0.025
Platinum	5.00	10×10^{-6}	0.050	0.051
Silver	4.50	1.63×10^{-6}	0.015	0.022

Rubens theory estimates secondary surface properties like the spectral normal emissivity fairly well.

2.6 Chapter Summary

This chapter begins by reviewing the blackbody model of radiation heat transfer and the concept of the solid angle. Using these basic concepts, a simple Earth radiation budget is constructed to obtain the effective blackbody temperature of the Earth. In Chapter 3, the importance of the effective blackbody temperature of the Earth will become apparent. The remaining sections introduce the electrical resistivity and the complex index of refraction, important parameters for describing the propagation of electromagnetic waves in conducting media, which is the subject of the next chapter.

Chapter 3

Propagation of Electromagnetic Waves Through Solids

This chapter uses the concepts introduced in Chapter 2 to derive a volumetric heat generation and reflection model for the absorber layer. The first section establishes a relationship between electric field magnitude and the blackbody intensity. Section 3.2 describes the behavior of radiation arriving at a plane boundary. The volumetric heat generation models for two cases, that of a semi-infinite medium and that of a second-surface mirror, are derived in Section 3.3. Finally a reflection model is derived in Section 3.4. Both the heat generation and reflection models are derived from electromagnetic theory.

3.1 Energy Carried by Electromagnetic Waves

Electromagnetic (EM) waves transport energy. As the electromagnetic wave propagates through space, it can give up some of its energy to material objects encountered along its

path. The instantaneous rate of energy flow associated with an EM wave is given by the Poynting vector,

$$\tilde{\mathbf{S}} = \tilde{\mathbf{E}} \times \tilde{\mathbf{H}} \ . \tag{3.1}$$

For the case of a y-polarized harmonic EM wave propagating along the x-axis, the instantaneous electric field is

$$\tilde{\mathbf{E}} = \mathbf{E}e^{i\phi_E} = E_y \mathbf{j} e^{i\phi_E} \tag{3.2}$$

and instantaneous magnetic field intensity is

$$\tilde{\mathbf{H}} = \mathbf{H}e^{i\phi_H} = H_z \mathbf{k} e^{i\phi_H} \ . \tag{3.3}$$

In Equations 3.2 and 3.3, ϕ_E and ϕ_H are the phase angles defined in Appendix A.

The Poynting vector has units of W/m^2 and it represents power per unit normal area to the direction of propagation of the EM wave, as indicated in Figure 3.1. The instantaneous amplitude of $\tilde{\mathbf{S}}$ for the plane electromagnetic wave in the current example is

$$\mathbf{S} = \|\tilde{E}_y \tilde{H}_z\| \mathbf{i} \ , \tag{3.4}$$

where $\tilde{E}_y = E_y e^{i\phi_E}$ and $\tilde{H}_z = H_z e^{i\phi_H}$ are complex scalars. The operation $\| \ \|$ gives the magnitude of the complex product of $\tilde{E}_y$ and $\tilde{H}_z$ as described in Appendix A.

We can simplify Equation 3.4 further by taking advantage of the fact that [Seigel and Howell, 1992]

$$\tilde{H}_z = \frac{\tilde{n}\tilde{E}_y}{\mu c_0} \ . \tag{3.5}$$

For diamagnetic materials such as air and the absorber materials under study in this thesis $\mu \cong \mu_0$ and both $\tilde{n}$ and $\tilde{E}_y$ are generally complex. The quantity $\mathrm{Z}_0 = \mu_0 c_0$ is known as

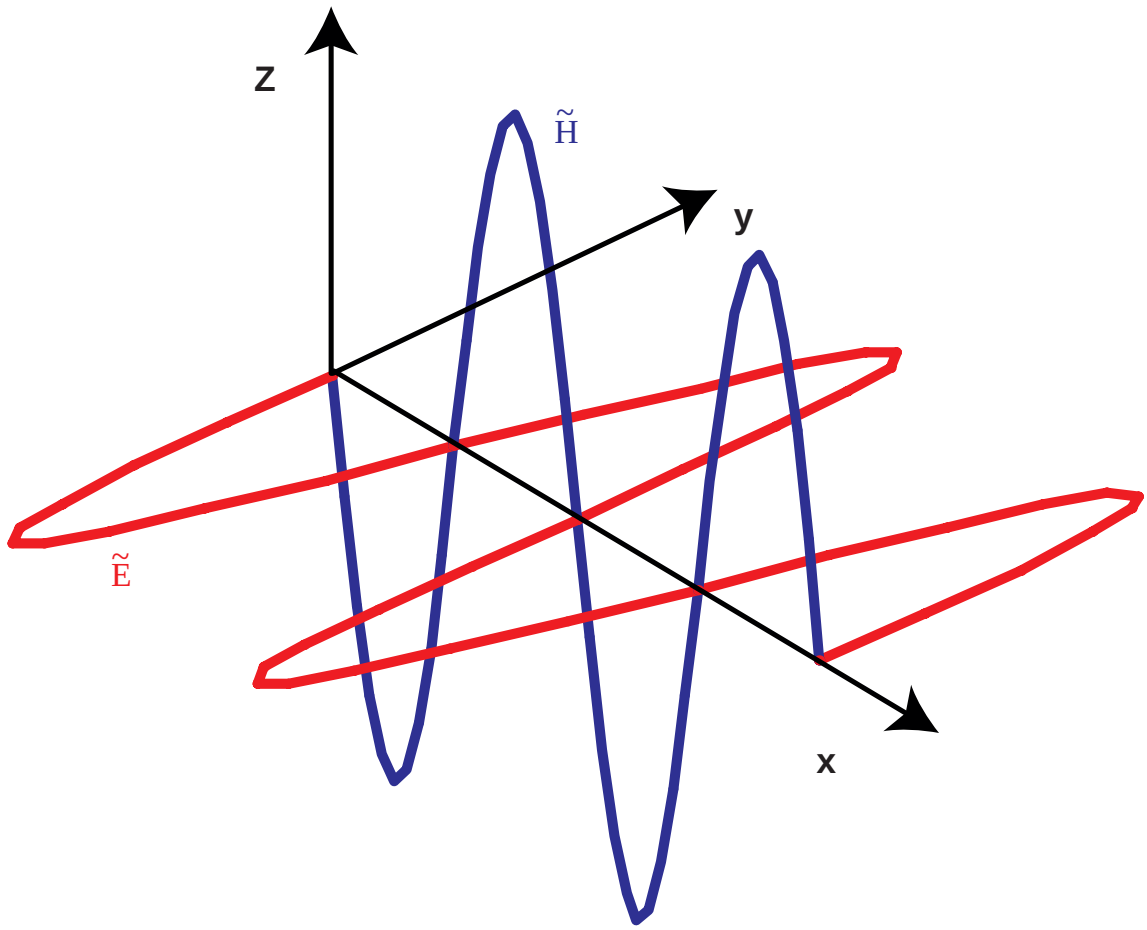

Figure 3.1: A y-polarized harmonic EM wave propagating in the x-direction.

the intrinsic impedance of free space and is approximately equal to 377 Ω. Then with the simplification afforded by Equation 3.5, Equation 3.4 becomes

$$S = \| \, |\tilde{\mathbf{S}}| \, \| = \left\| \frac{\tilde{n}\tilde{E}_y^2}{\mu_0 c_0} \right\| \ , \tag{3.6}$$

where the operator $|\tilde{\mathbf{S}}|$ is equal to $\tilde{S}$, the complex magnitude of the Poynting vector, as explained in Appendix A. Note that under the assumption of a time harmonic EM wave, $\mathbf{S}$ is also time harmonic.

Equation 3.6 describes the instantaneous power flux carried by the harmonic EM wave. A more useful quantity for a plane electromagnetic wave is the average power flux over time since the average power flux over time, or the wave intensity. Equation 3.6 may be expressed in terms of the average power flux as

$$S_{avg} = \left\| \frac{\tilde{n} \int_0^P \tilde{E}_y^2 dt}{P \mu_0 c_0} \right\| = \left\| \frac{\tilde{n}\tilde{E}_{max}^2}{2\mu_0 c_0} \right\| \ , \tag{3.7}$$

where $\tilde{E}_{max}$ in this case is the amplitude and P is the period of the electric field. If the medium is air or vacuum, then $\tilde{n}$ is real and equal to unity. Equation 3.7 has been derived for a linearly polarized wave. In Section 3.2, it is shown that for normal incidence, the result is equally valid for natural radiation, which is randomly polarized.

The power flux arriving at the satellite in wavelength interval $\Delta\lambda$ centered on wavelength λ_0 is

$$S_{avg} = \int_{\lambda_0 - \Delta\lambda/2}^{\lambda_0 + \Delta\lambda/2} \frac{\omega c_1}{\lambda^5 [e^{c_2/(\lambda T)} - 1]} d\lambda \ . \tag{3.8}$$

It is very difficult to analytically integrate the Planck function over a finite wavelength interval. Therefore, it is convenient to approximate the Planck function using Wien's function;

that is,

$$S_{avg} = \int_{\lambda_0-\Delta\lambda/2}^{\lambda_0+\Delta\lambda/2} \frac{\omega c_1}{\lambda^5 e^{c_2/\lambda T}} d\lambda \ . \tag{3.9}$$

This convenient approximation incurs minimal error the Planck function with Wien's function is small as shown in Figure 2.1.

Carrying out the indicated integration yields

$$\|\tilde{S}_{avg}\| = \frac{\omega c_1}{e^{c_2/\lambda T}} \left(\frac{6T^4}{c_2^4} + \frac{6T^3}{c_2^3\lambda} + \frac{3T^2}{c_2^2\lambda^2} + \frac{T}{c_2\lambda^3} \right) \Big|_{\lambda_0-\Delta\lambda/2}^{\lambda_0+\Delta\lambda/2} \ . \tag{3.10}$$

Now the amplitude of the electric field can be expressed in terms of the result from Equation 3.10; that is,

$$\|\tilde{E}_{max}(\lambda_0, \Delta\lambda, T)\| = \sqrt{\frac{2\omega\mu_0 c_0 c_1}{e^{c_2/(\lambda T)}} \left(\frac{6T^4}{c_2^4} + \frac{6T^3}{c_2^3\lambda} + \frac{3T^2}{c_2^2\lambda^2} + \frac{T}{c_2\lambda^3} \right) \Big|_{\lambda_0-\Delta\lambda/2}^{\lambda_0+\Delta\lambda/2}} \ . \tag{3.11}$$

It must be noted that the electric field on distance, x, comes from the definition of the solid angle. This is because the solid angle depends on the geometry between the Earth and the satellite. Since, in this thesis the solid angle is a constant, the dependancy on distance is not included in Equation 3.11

3.2 Harmonic Electromagnetic Waves Arriving at a Plane Boundary

As an EM wave passes from one medium to another, the difference between the electrical impedance of the two media causes it to be partially reflected and partially transmitted. This is illustrated in Figures 3.2 and 3.3. We can find how much of the incident EM wave

is reflected by applying the principle of conservation of energy, which leads indirectly to expressions for the conservation of electric and magnetic field strength at an interface.

From conservation of energy we have

$$\|\tilde{S}_{in}\| = \|\tilde{S}_r\| + \|\tilde{S}_t\| \ , \tag{3.12}$$

where

$$\tilde{S} = Se^{i\phi} \tag{3.13}$$

so that

$$\|\tilde{S}\| = S \ . \tag{3.14}$$

Using Equation 3.6, we can rewrite Equation 3.12 as

$$\left\| \frac{\tilde{n}_0 \tilde{E}_{in}^2}{\mu_0 c_0} \right\| = \left\| \frac{\tilde{n}_0 \tilde{E}_r^2}{\mu_0 c_0} \right\| + \left\| \frac{\tilde{n}_1 \tilde{E}_t^2}{\mu c_0} \right\| \ . \tag{3.15}$$

We can then make use of the fact that $\mu_0 \cong \mu$ for diamagnetic media to eliminate the factor $\mu_0 c_0$ from Equation 3.15. If the incident radiation is in a vacuum or air, then $\tilde{E}_{in} = E_{max}(\lambda_0, \Delta\lambda, T, x)e^{i\phi_E}$. The phase angle, ϕ_E, can be arbitrarily chosen and so for convenience it is chosen to be zero.

Let us consider normal incidence for the two general cases: a conductor and a dielectric.

3.2.1 Normal Incidence at a Dielectric Boundary

Consider Figure 3.2. From the principle of conservation of electric and magnetic field strength at the interface [Cheng, 1992] we can write in vector notation

$$\tilde{\mathbf{E}}_{in} + \tilde{\mathbf{E}}_r = \tilde{\mathbf{E}}_t \tag{3.16}$$

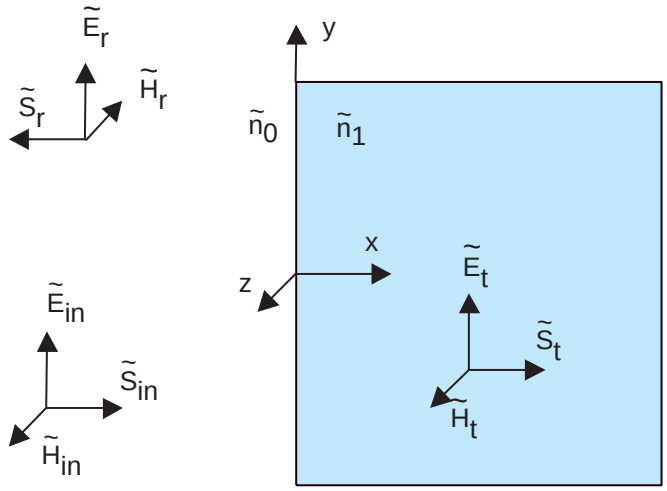

Figure 3.2: Normal Incidence of a harmonic EM wave on a plane dielectric interface bounding media having different indices of refraction.

and

$$\tilde{\mathbf{H}}_{in} + \tilde{\mathbf{H}}_r = \tilde{\mathbf{H}}_t \ . \tag{3.17}$$

Rewriting Equations 3.16 and 3.17 as magnitudes and introducing electrical impedance and magnitude of electric field strength we have

$$|\tilde{\mathbf{E}}_{in}| + |\tilde{\mathbf{E}}_r| = |\tilde{\mathbf{E}}_t| \tag{3.18a}$$

or

$$\tilde{E}_{in} + \tilde{E}_r = \tilde{E}_t \ . \tag{3.18b}$$

and

$$\frac{|\tilde{\mathbf{E}}_{in}| - |\tilde{\mathbf{E}}_r|}{Z_0} = \frac{|\tilde{\mathbf{E}}_t|}{\tilde{Z}_1} \tag{3.19a}$$

or

$$\frac{\tilde{E}_{in} - \tilde{E}_r}{Z_0} = \frac{\tilde{E}_t}{\tilde{Z}_1} \ . \tag{3.19b}$$

The ratios $\tilde{E}_r/\tilde{E}_{in}$ and $\tilde{E}_t/\tilde{E}_{in}$ are called the reflection and transmission coefficients, respectively. They can be calculated using Equations 3.18a and 3.19a. In terms of electrical impedance the reflection and transmission coefficients may be written

$$\tilde{\Gamma} = \frac{\tilde{E}_r}{\tilde{E}_{in}} = \frac{\tilde{Z}_1 - Z_0}{\tilde{Z}_1 + Z_0} \tag{3.20}$$

and

$$\tilde{\tau} = \frac{\tilde{E}_t}{\tilde{E}_{in}} = \frac{2\tilde{Z}_1}{\tilde{Z}_1 + Z_0} \ . \tag{3.21}$$

Note that in Equations 3.19a through 3.21 the characteristic impedance of free space Z_0 is real, but the impedance of medium 1, $\tilde{Z}_1$, may be complex. The impedance of a given material is given by $\tilde{Z} = \mu c_0/\tilde{n}$. Also, recall that for diamagnetic media, $\mu_0 \cong \mu$. Therefore, in terms of complex index of refraction, the reflection and transmission coefficient may be expressed as

$$\tilde{\Gamma} = \frac{\tilde{E}_r}{\tilde{E}_{in}} = \frac{\tilde{n}_0 - \tilde{n}_1}{\tilde{n}_0 + \tilde{n}_1} \tag{3.22}$$

and

$$\tilde{\tau} = \frac{\tilde{E}_t}{\tilde{E}_{in}} = \frac{2\tilde{n}_0}{\tilde{n}_0 + \tilde{n}_1} \ . \tag{3.23}$$

The reflection coefficient, $\tilde{\Gamma}$, can be positive or negative depending on the magnitudes of the complex indices of refraction. The transmission coefficient is always positive. Reflection and transmission coefficients are related by

$$1 + \tilde{\Gamma} = \tilde{\tau} \ , \tag{3.24}$$

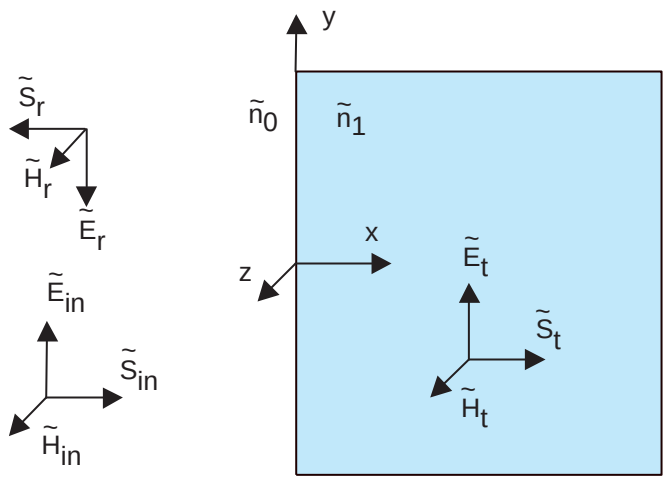

Figure 3.3: Normal Incidence of an EM wave on a plane conducting interface bounding media having different indices of refraction.

which makes it clear that the imaginary part of transmission coefficient is the same as the imaginary part of the reflection coefficient.

3.2.2 Normal Incidence at a Conducting Boundary

Now consider the conductor in Figure 3.3. The conservation of electric and magnetic field strength remain unchanged; this is,

$$\tilde{\mathbf{E}}_{in} + \tilde{\mathbf{E}}_r = \tilde{\mathbf{E}}_t \tag{3.25}$$

and

$$\tilde{\mathbf{H}}_{in} + \tilde{\mathbf{H}}_r = \tilde{\mathbf{H}}_t \ . \tag{3.26}$$

Since the physics of the problem has not changed the development in Section 3.2.1 can be applied to conducting media as well. If the conductor in Figure 3.3 was a perfect conductor,

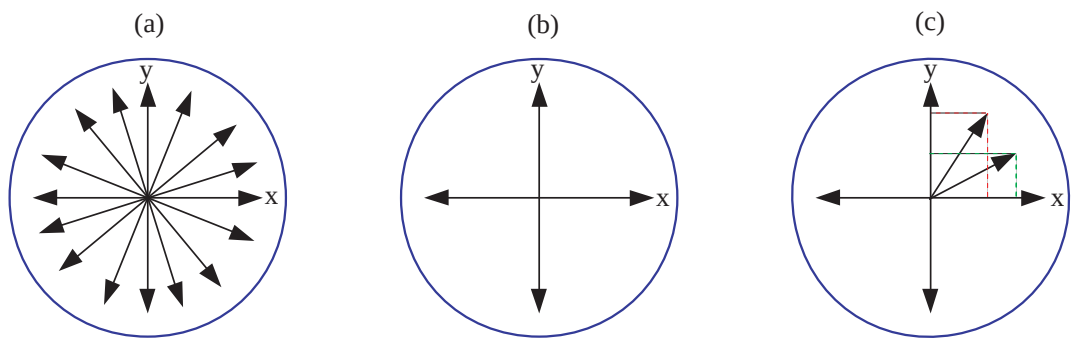

Figure 3.4: (a) Components of a randomly, or naturally, polarized electric field, (b) two orthogonal linearly polarized electric fields and (c) resolution of two electric field components into their two orthogonal components.

we know from intuition that it will reflect all incident radiation and none will be transmitted. Equations 3.20 and 3.21 will in fact predict this outcome since the impedance of a perfect conductor is zero.

3.2.3 Reflectance and Transmittance at a Plane Boundary

The electric components of an unpolarized, or "natural", beam of radiation, shown in Figure 3.4(a), can be resolved into two equal orthogonal components, Figure 3.4(b). This is done by resolving each electric field making up the randomly polarized radiation into two orthogonal components, as shown in Figure 3.4(c).

Now the reflectivity, ρ, at an interface is defined

$$\rho \equiv \frac{\tilde{E}_r \tilde{E}_r^*}{\tilde{E}_{in} \tilde{E}_{in}^*} \ , \tag{3.27}$$

and the transmissivity, $\overline{\tau}$, at an interface is defined

$$\overline{\tau} \equiv \frac{\tilde{E}_t \tilde{E}_t^* \tilde{n}_1}{\tilde{E}_{in} \tilde{E}_{in}^* \tilde{n}_0} = 1 - \rho \ . \tag{3.28}$$

It must the stressed that $\overline{\tau}$ is defined for an interface and so it is different from the transmissivity defined for a finite length.

The reflectivity ρ for randomly polarized radiation is the average of that due to the x and y components into which the incident electric fields have been resolved; that is

$$\rho = \frac{\rho_x + \rho_y}{2} \ . \tag{3.29}$$

We can see that for the case of normal incidence, $\rho_x = \rho_y$, so that

$$\rho = \rho_x = \rho_y \ . \tag{3.30}$$

Like the reflectivity, the transmissivity, $\tilde{\tau}$ for naturally polarized radiation can be resolved into two components; that is,

$$\overline{\tau} = \frac{\overline{\tau}_x + \overline{\tau}_y}{2} \ . \tag{3.31}$$

Thus we see that for the case of normal incidence, $\overline{\tau} = \overline{\tau}_x = \overline{\tau}_y$.

3.3 Absorption of Radiation by a Conducting Medium

The band-averaged electric field component of a y-polarized harmonic electromagnetic wave has the form

$$\tilde{E}_y(x, \nu_0, \Delta\lambda, T, t) \cong \tilde{E}_t(\nu_0, \Delta\lambda, T) e^{2\pi i \nu_0 (t - x/c_0)} \ , \tag{3.32a}$$

or

$$\tilde{E}_y(x, \nu_0, \Delta\lambda, T, t) \cong \|\tilde{E}_t(\nu_0, \Delta\lambda, T)\| e^{i[2\pi\nu_0(t-x/c_0)+\phi]} \ , \tag{3.32b}$$

where $\tilde{E}_t(\Delta\lambda, T)$ is the transmitted electric field, ν_0 is the frequency in hertz, t is the time in seconds, x is the distance in meters, and ϕ is the phase angle as defined in Appendix A. Equations 3.32a and 3.32b expresses an approximate equality because the behavior they attribute to the transmitted electric field is that of a monochromatic wave whose frequency is ν_0 rather than that of the actual band of waves of bandwidth $\Delta\lambda$ centered about $\lambda_0 = c_0/\nu_0$. In terms of the real index of refraction of the medium, n, Equation 3.32a may be written

$$\tilde{E}_y(x, \nu_0, \Delta\lambda, T, t) \cong \tilde{E}_t(\lambda_0, \Delta\lambda, T) e^{2\pi i\nu_0(t-nx/c_0)} \ . \tag{3.33}$$

When an EM wave enters a conducting medium (i.e. a medium having finite resistivity), it will begin to convert some of its energy into sensible heat. Mathematically, radiation absorbed in this material can be represented by an exponentially decreasing attenuating factor. Incorporating the attenuating factor in Equation 3.33 yields

$$\tilde{E}_y(x, \nu_0, \Delta\lambda, T) \cong \tilde{E}_t(\lambda_0, \Delta\lambda, T) \left[e^{2\pi i\nu_0(t-nx/c_0)}\right] \left[e^{-2\pi\nu_0\kappa x/c_0}\right] \ , \tag{3.34}$$

where κ is the extinction coefficient, which can be thought of as the imaginary part of the complex index of refraction. The resulting behavior of the propagating electric field is shown in Figure 1.4. The time dependance of this equation can be eliminated for the case of a harmonic function of time by considering only the root-mean-square value,

$$\tilde{E}_y(x, \nu_0, \Delta\lambda, T) \cong \frac{\tilde{E}_t(\lambda_0, \Delta\lambda, T)}{\sqrt{2}} \left[e^{-2\pi i\nu_0 nx/c_0}\right] \left[e^{-2\pi\nu_0\kappa x/c_0}\right] \ . \tag{3.35}$$

Since $\nu_0 = c_0/\lambda_0$, Equation 3.35 can be rewritten as

$$\tilde{E}_y(x, \lambda_0, \Delta\lambda, T) \cong \frac{\tilde{E}_t(\lambda_0, \Delta\lambda, T)}{\sqrt{2}} \left[e^{-2\pi inx/\lambda_0}\right] \left[e^{-2\pi\kappa x/\lambda_0}\right] \ . \tag{3.36}$$

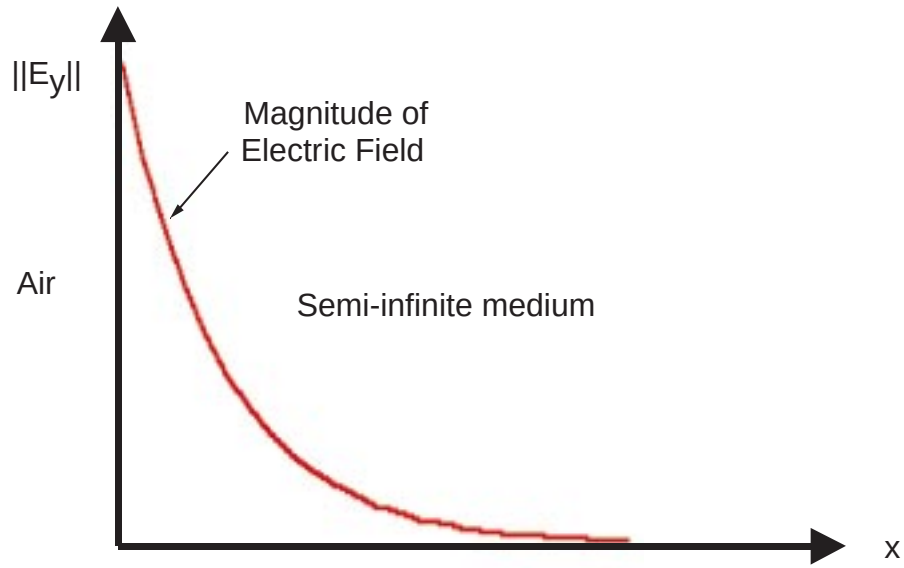

Figure 3.5: Absorption of an EM wave propagating in a semi-infinite medium.

Finally, simplifying Equation 3.36 yields

$$\tilde{E}_y(x, \lambda_0, \Delta\lambda, T) \cong \frac{\tilde{E}_t(\lambda_0, \Delta\lambda, T)}{\sqrt{2}} e^{-2\pi i x(n - i\kappa)/\lambda_0} \ . \tag{3.37}$$

Equation 3.37 is limited to semi-infinite media, such as that illustrated in Figure 3.5.

An electric field incident to the medium produces a local current density,

$$\tilde{\mathbf{J}} = \frac{\tilde{\mathbf{E}}_{\mathbf{y}}}{r_e} \ , \tag{3.38}$$

where $\tilde{\mathbf{J}}$ is the current density in amps per meter squared and r_e is the electrical resistivity in ohm·meters. Conversion of electrical energy into heat is given by

$$\dot{g}(x, \lambda_0, \Delta\lambda, T) = \tilde{\mathbf{J}} \cdot \tilde{\mathbf{E}} = \frac{\tilde{\mathbf{E}}_y \cdot \tilde{\mathbf{E}}_y^*}{r_e} = \frac{\|\tilde{E}_y\|^2}{r_e} \ , \tag{3.39}$$

where $\dot{g}$ is the volumetric heat generation in watts per meter cubed and $\tilde{\mathbf{E}}^*$ is the complex conjugate of the electric field, $\tilde{\mathbf{E}}$. The fact that $\tilde{\mathbf{E}}_y \cdot \tilde{\mathbf{E}}_y^* = \|\tilde{E}_y\|^2$ is developed in Appendix A.

Combining Equations 3.37 and 3.39, yields

$$\dot{g}(x, \lambda_0, \Delta\lambda, T) \cong \frac{\|\tilde{E}_t(\lambda_0, \Delta\lambda, T)\|^2}{2r_e} \left[e^{-2\pi i x(n-i\kappa)/\lambda_0}\right] \left[e^{-2\pi i x(n-i\kappa)/\lambda_0}\right]^* \ . \tag{3.40}$$

3.3.1 Volumetric Heat Generation by an Electromagnetic Wave in a Semi-infinite Medium

Employing Euler's identity,

$$e^{i\theta} = \cos\theta + i\sin\theta \ , \tag{3.41}$$

Equation 3.40 can be rewritten as

$$\dot{g}(x, \lambda_0, \Delta\lambda, T) \cong \frac{\|\tilde{E}_t(\lambda_0, \Delta\lambda, T)\|^2}{2r_e} \left[e^{-2\pi\kappa x/\lambda_0}(\cos\frac{-2\pi n x}{\lambda_0} + i\sin\frac{-2\pi n x}{\lambda_0})\right] \left[e^{-2\pi\kappa x/\lambda_0}(\cos\frac{-2\pi n x}{\lambda_0} - i\sin\frac{-2\pi n x}{\lambda_0})\right] \ . \tag{3.42}$$

Simplifying, there results

$$\dot{g}(x, \lambda_0, \Delta\lambda, T) \cong \frac{\|E_t(\lambda_0, \Delta\lambda, T)\|^2}{2r_e} \left[e^{2(-2\pi\kappa x/\lambda_0)}(\cos^2\frac{-2\pi n x}{\lambda_0} + \sin^2\frac{-2\pi n x}{\lambda_0})\right] \ . \tag{3.43}$$

Now introducing the well-known trigonometric identity

$$\cos^2\theta + \sin^2\theta = 1 \ , \tag{3.44}$$

Equation 3.43 simplifies to

$$\dot{g}(x, \lambda_0, \Delta\lambda, T) \cong \frac{\|\tilde{E}_t(\lambda_0, \Delta\lambda, T)\|^2}{2r_e} e^{-4\pi\kappa x/\lambda_0} \ . \tag{3.45}$$

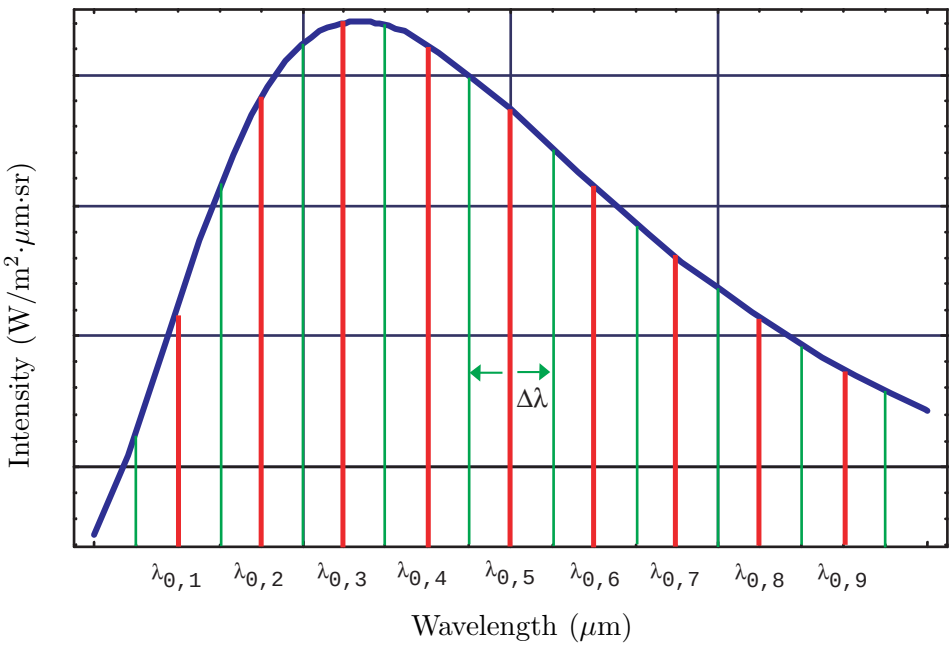

Figure 3.6: Division of Wien's function into bands.

Finally, summing over an arbitrary wavelength interval we obtain the volumetric heat generation as a function of penetration depth only,

$$\dot{g}(x,T) \cong \sum_{m=1}^{M_{max}} \frac{\|\tilde{E}_t(\lambda_{0,m}, \Delta\lambda, T)\|^2}{2r_e} e^{-4\pi\kappa x/\lambda_{0,m}} \ , \tag{3.46}$$

where the parameter M_{max} denotes the number of central wavelengths in the interval, $\lambda_{0,m} = \lambda_{0,1} + (m-1)\Delta\lambda$, as illustrated in Figure 3.6. Even though the ordinate in Figure 3.6 is intensity, it can also be electric field, since we know from Equation 3.11 intensity is proportinal to the electric field squared.

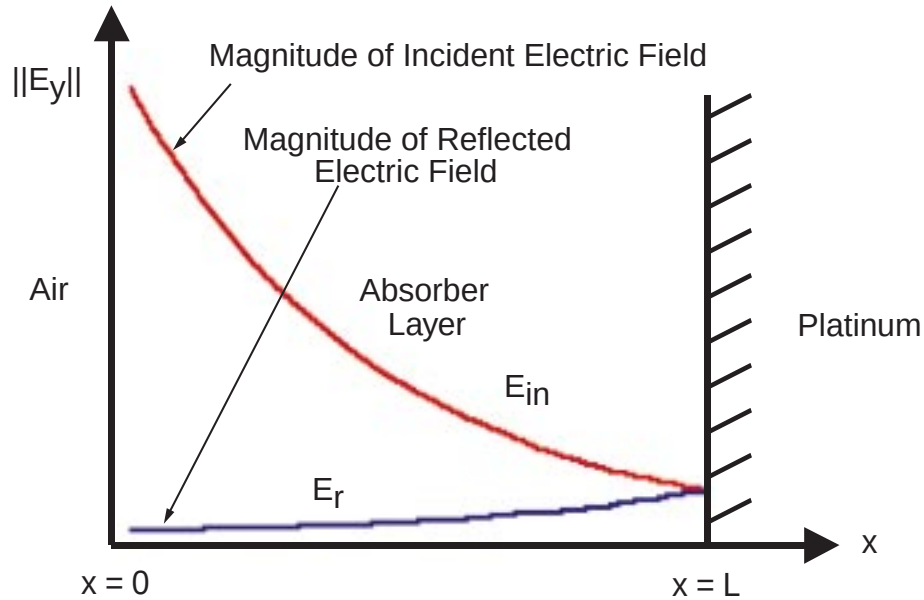

Figure 3.7: Attenuation of a harmonic EM wave propagating in a second-surface mirror.

3.3.2 Volumetric Heat Generation due to a Harmonic Electromagnetic Wave Propagating Within a Second-Surface Mirror

A second-surface mirror consists of a semi-transparent coating applied to a reflective substrate, as illustrated in Figure 3.7. Radiation incident to a second-surface mirror is split into two beams, one which is reflected from the outer surface of the coating and the other of which is reflected from the substrate. The absorber layer bonded to the platinum substrate in the current application acts as a second-surface mirror. The equations in the previous sub-section must be modified to include the electromagnetic wave that is reflected at the absorber-platinum interface, as illustrated in Figure 3.7. Rewriting Equation 3.39 to include the reflected electromagnetic wave yields

$$\dot{g}(x, \lambda_0, \Delta\lambda, T) = \tilde{\mathbf{J}} \cdot \tilde{\mathbf{E}} = \frac{\|\mathbf{E}\|^2}{r_e} = \frac{(\tilde{\mathbf{E}}_{\mathbf{in}} + \tilde{\mathbf{E}}_{\mathbf{r}}) \cdot (\tilde{\mathbf{E}}^*_{\mathbf{in}} + \tilde{\mathbf{E}}^*_{\mathbf{r}})}{r_e} \ , \tag{3.47}$$

where $\tilde{\mathbf{E}}_{\mathbf{in}}$ is the incident electric field and $\tilde{\mathbf{E}}_{\mathbf{r}}$ is the reflected electric field.

Platinum has a normal reflectance of 0.976 at 10 μm and 0.945 at 5 μm [Lide, 1998]. Therefore, in this thesis it is assumed that a vapor deposited platinum layer is a perfectly reflecting material (i.e. a perfect conductor). Then, applying conservation of the electric field at the interface, Equation 3.18a, we have

$$\tilde{E}_{in} + \tilde{E}_r = \tilde{E}_t = 0 \ , \tag{3.48}$$

since $\tilde{E}_t$, the transmitted electric field, is zero. Therefore, the reflected field is

$$\tilde{E}_r = -\tilde{E}_{in} \ . \tag{3.49}$$

This condition is strictly valid only for both normal and specular reflection at the interface. Equation 3.49 implicitly states that heat generation at the interface is zero because the net electric field there is zero.

The reflected electric field may be represented mathematically by

$$\tilde{E}_{y,r}(x, \lambda_0, \Delta\lambda, T) \cong \frac{-\tilde{E}_t(\Delta\lambda, T)}{\sqrt{2}} \left[e^{2\pi i x(n-i\kappa)/\lambda_0}\right] \left[e^{-4\pi i \ell(n-i\kappa)/\lambda_0}\right] \ , \tag{3.50}$$

where ℓ is the depth of the absorber layer. Once again, the approximation comes about because $\Delta\lambda$ is a finite bandwidth centered about wavelength λ_0.

When the "incident" (transmitted) electric field given by Equation 3.37 and the reflected electric field given by Equation 3.50 are introduced into Equation 3.47

$$\dot{g}(x, \lambda_0, \Delta\lambda, T) \cong \frac{\|\tilde{E}_t(\lambda_0, \Delta\lambda, T)\|^2}{2r_e} e^{-4\pi\kappa(2\ell+x)/\lambda_0} \left[e^{8\pi\kappa\ell/\lambda_0} + e^{8\pi\kappa x/\lambda_0} - 2e^{4\pi\kappa(\ell+x)/\lambda_0} \cos\frac{4\pi n(\ell - x)}{\lambda_0}\right] \ . \tag{3.51}$$

The derivation is quite lengthy and tedious and therefore is relegated to Appendix B.

In order to find the total heat generation rate, we sum Equation 3.51 over the wavelength interval interested in, as in Equation 3.46; that is,

$$\dot{g}(x,T) = \sum_{m=1}^{M_{max}} \dot{g}(x, \lambda_{0,m}, \Delta\lambda, T) \ . \tag{3.52}$$

3.3.3 Convergence of the Volumetric Heat Generation Equations

Equation 3.51 must converge to Equation 3.45 as the thickness approaches infinity. In order to verify this, we take the limit of Equation 3.51 as ℓ approaches infinity. First, combining the exponential factors, Equation 3.51 may be written

$$\dot{g}(x, \lambda_0, \Delta\lambda, \ell, T) \cong \frac{\|\tilde{E}_t(\lambda_0, \Delta\lambda, T)\|^2}{2r_e}$$
$$\left[e^{-4\pi(2\ell+x)\kappa/\lambda_0} e^{8\pi\ell\kappa/\lambda_0} + e^{-4\pi(2\ell+x)\kappa/\lambda_0} e^{8\pi x\kappa/\lambda_0} - 2e^{-4\pi(2\ell+x)\kappa/\lambda_0} e^{4\pi(\ell+x)\kappa/\lambda_0} \cos\frac{4\pi n(\ell - x)}{\lambda_0}\right] \ , \tag{3.53}$$

which upon simplification becomes

$$\dot{g}(x, \lambda_0, \Delta\lambda, , \ell, T) \cong \frac{\|\tilde{E}_t(\lambda_0, \Delta\lambda, T)\|^2}{2r_e}$$
$$\left[e^{-4\pi x\kappa/\lambda_0} + e^{-8\pi\ell\kappa/\lambda_0} e^{-4\pi x\kappa/\lambda_0} - 2e^{-4\pi\ell\kappa/\lambda_0} \cos\frac{4\pi n(\ell - x)}{\lambda_0}\right] \ . \tag{3.54}$$

Clearly if $\ell \to \infty$, Equation 3.54 converges to

$$\dot{g}(x, \lambda_0, \Delta\lambda, , T) \cong \frac{\|\tilde{E}_t(\lambda_0, \Delta\lambda, T)\|^2}{2r_e} e^{-4\pi\kappa x/\lambda_0} \ , \tag{3.55}$$

which is identical to Equation 3.45.

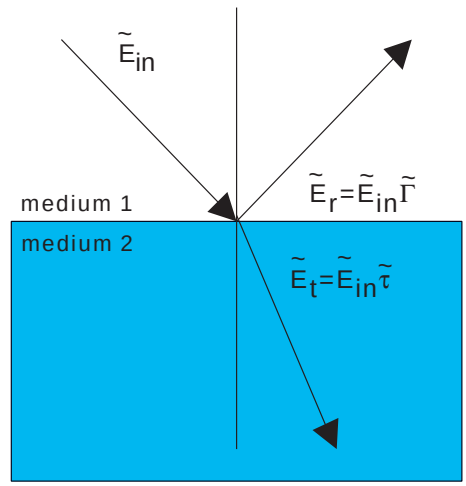

Figure 3.8: Reflection and transmission of an incident electric wave by an ideal surface.

3.4 Reflection from the Surface of a Thin Film

Having developed the equations for the volumetric absorption of radiation within a thin film from electromagnetic theory, we are now ready to derive an expression describing net reflection of radiation from the upper surface of the absorber layer.

3.4.1 Stokes Reflection and Refraction

The British physicist Sir George Stokes developed a unique way of treating reflection at a plane boundary [Hecht and Zajac, 1974]. As illustrated in Figure 3.8,

$$\tilde{E}_{in} = \tilde{E}_r + \tilde{E}_t = \tilde{E}_{in}\tilde{\Gamma} + \tilde{E}_{in}\tilde{\tau} \ . \tag{3.56}$$

Now, imagine that all the ray directions are reversed, as in Figure 3.9. Changing the direction

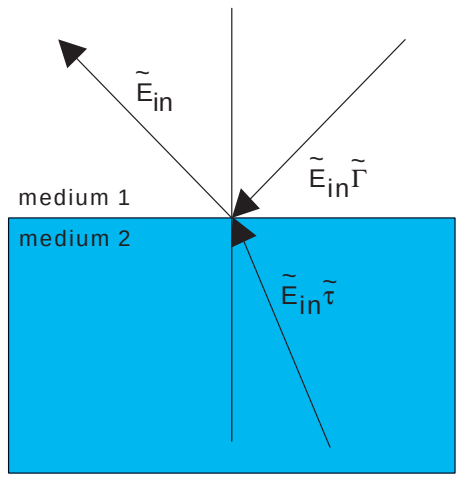

Figure 3.9: Reversed reflection and transmission by an ideal surface.

of rays does not alter the physics, so Equation 3.56 is still valid.

We then treat the reflected and transmitted rays individually, as illustrated in Figure 3.10.

The governing equation for the refraction and reflection of radiation for the situation illustrated in Figure 3.10(a) can be written as

$$\tilde{E}_{in}\tilde{\tau} = \tilde{E}_{in}\tilde{\tau}\tilde{\tau}' + \tilde{E}_{in}\tilde{\tau}\tilde{\Gamma} \ , \tag{3.57}$$

where $\tilde{\tau}'$ is the transmission coefficient from medium 2 to medium 1. At this time it is important to point out that $\tilde{\tau}'$ is not equal to $\tilde{\tau}$. Referring to Figure 3.10(b), we can also write

$$\tilde{E}_{in}\tilde{\Gamma} = \tilde{E}_{in}\tilde{\Gamma}\tilde{\Gamma} + \tilde{E}_{in}\tilde{\Gamma}\tilde{\tau} \ . \tag{3.58}$$

Since the physics reprensented in Figures 3.10(a) and 3.10(b) must be the same as that in Figure 3.9, then we can write

$$\tilde{E}_{in} = \tilde{E}_{in}\tilde{\Gamma}\tilde{\Gamma} + \tilde{E}_{in}\tilde{\tau}\tilde{\tau}' \ , \tag{3.59}$$

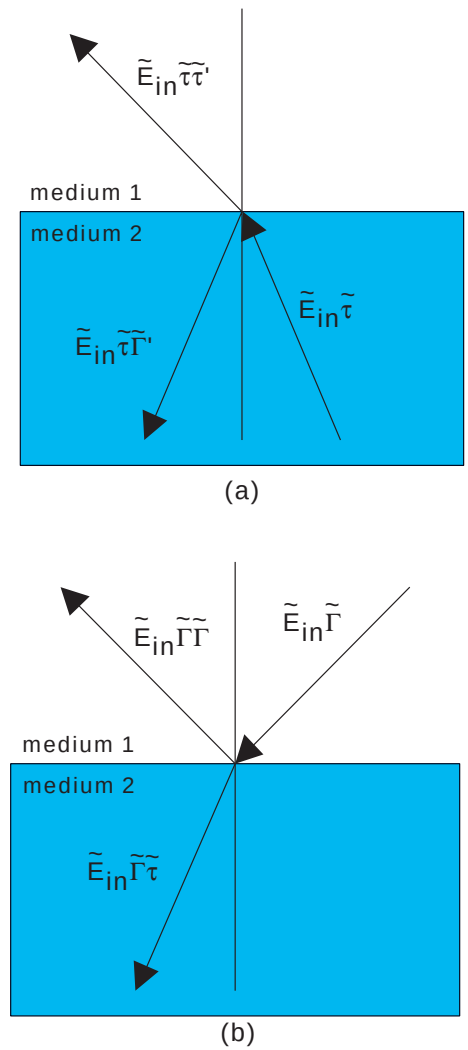

Figure 3.10: Illustration of Stokes reflection: (a) reflection and transmission of the transmitted ray and (b) reflection and transmission of the reflected ray.

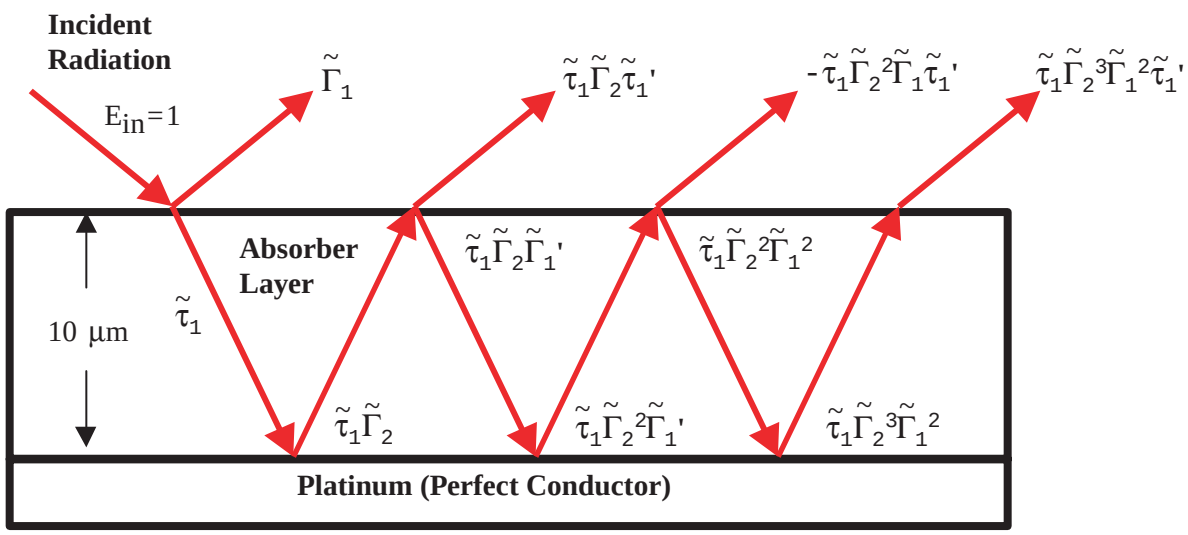

Figure 3.11: Schematic diagram of multiple reflections at the interfaces of a thin film with its surroundings.

from which we conclude that

$$\tilde{\tau}\tilde{\tau}' = 1 - \tilde{\Gamma}^2 \ . \tag{3.60}$$

Furthermore, we can also write that

$$\tilde{E}_{in}\tilde{\Gamma}\tilde{\tau} + \tilde{E}_{in}\tilde{\tau}\tilde{\Gamma}' = 0, \tag{3.61}$$

which leads to the conclusion that

$$\tilde{\Gamma}' = -\tilde{\Gamma} \ . \tag{3.62}$$

3.4.2 Reflection from Second-Surface Mirrors

The absorber layer can be modeled as a second-surface mirror, as illustrated in Figure 3.11. This figure suggests that the amplitude of the reflected electric field can be expressed

$$\tilde{E}_r = \tilde{E}_{in}\tilde{\Gamma}_1 + \tilde{E}_{in}\tilde{\tau}_1\tilde{\Gamma}_2\tilde{\tau}_1' e^{-4\pi i\ell(n-i\kappa)/\lambda_0} - \tilde{E}_{in}\tilde{\tau}_1\tilde{\Gamma}_2^2\tilde{\Gamma}_1\tilde{\tau}_1' e^{-8\pi i\ell(n-i\kappa)/\lambda_0} + ... \quad . \tag{3.63}$$

Recalling that reflectivity is defined as

$$\rho \equiv \frac{\tilde{E}_r\tilde{E}_r^*}{\tilde{E}_{in}\tilde{E}_{in}^*} \ , \tag{3.64}$$

we can write

$$\rho = \tilde{\Gamma}_1\tilde{\Gamma}_1^* + \tilde{\tau}_1^*\tilde{\tau}_1^{*\prime}\tilde{\Gamma}_1\tilde{\Gamma}_2^* e^{-4\pi\ell\tilde{n^*}/\lambda_0} + \tilde{\tau}_1\tilde{\tau}_1'\tilde{\Gamma}_2\tilde{\Gamma}_1^* e^{-4\pi\ell\tilde{n}/\lambda_0} + \tilde{\tau}_1\tilde{\tau}_1^*\tilde{\tau}_1'\tilde{\tau}_1^{*\prime}\tilde{\Gamma}_2\tilde{\Gamma}_2^* e^{-4\pi\ell\tilde{n}/\lambda_0} e^{-4\pi\ell\tilde{n^*}/\lambda_0} \ . \tag{3.65}$$

In writing Equation 3.65 we have assumed that reflection is dominated by the first two terms of Equation 3.64.

We now define the power transmittance as $\overline{T} = \tilde{\tau}\tilde{\tau}^*$ and the power reflectance as $\overline{R} = \tilde{\Gamma}\tilde{\Gamma}^*$.

Using Euler's identity and introducing the power reflectance and the power transmittance, we can simplify Equation 3.65 to

$$\rho = \overline{R}_1 + 2(\overline{T}_1'\overline{T}_1\overline{R}_1\overline{R}_2)^{0.5} e^{-4\pi\kappa\ell/\lambda_0} \cos\frac{4\pi n\ell}{\lambda_0} + \overline{T}_1\overline{T}_1'\overline{R}_2 e^{-8\pi\kappa\ell/\lambda_0} \ . \tag{3.66}$$

Reflectance models that take into consideration other factors such as the surface roughness also may be found in the literature; for example, that of Smith [1984].

3.5 Chapter Summary

In this chapter models for reflection and volumetric absorption of radiation are developed from electromagnetic theory. These are analytical models. In the next chapter an equivalent probabilistic model of heat generation is developed within an absorbing medium.

Chapter 4

Monte Carlo Method in Participating Media

This chapter presents an alternate way, the Monte Carlo ray-trace method, for determining the heat generation in the absorber layer. The first section gives some background information and describes how this approach was used in this thesis, and the remaining sections describe important concepts in the Monte Carlo ray-trace (MCRT) method in participating media: the absorption length, scattering, the distribution factor, and orphan rays.

4.1 Introduction

The MCRT method is a statistical numerical approach that mimics actual events by performing sampling experiments on a computer using pseudo-random numbers. In principle, the results of this approach are identical to the analytical solution. In many cases, the MCRT method is easier to use and less restrictive than the equivalent analytical approach. Also,

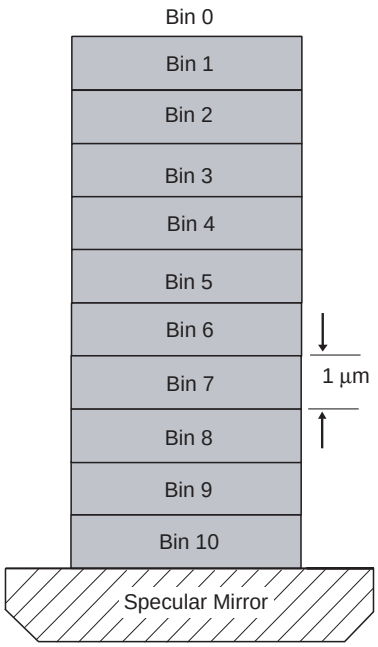

Figure 4.1: Division of the absorber layer into different bins.

with the increasing speed of computer processors, it requires less and less time to run an MCRT code. In any case the MCRT model is usually easier to formulate than the equivalent analytical model. The only caveat of the MCRT method is that one must perform lots of experiments ("ray traces") to obtain an accurate answer. Mahan [2000] recommends that for surface-to-surface radiation models at least 10,000n energy bundles be emitted from each surface element making up an enclosure. He adds that it is not uncommon in high accuracy applications to emit n $\times$ 10^6 energy bundles from each element.

In this work, an MCRT model is formulated for the absorber layer to obtain a "numerical" heat generation function. The absorber layer is divided into 10 equal volume elements, or bins, having a length of 1 μm each as illustrated by Figure 4.1. Energy bundles, or "rays", are fired from the top of the absorber layer toward the specular mirror. A copy of this code appears in Appendix D.

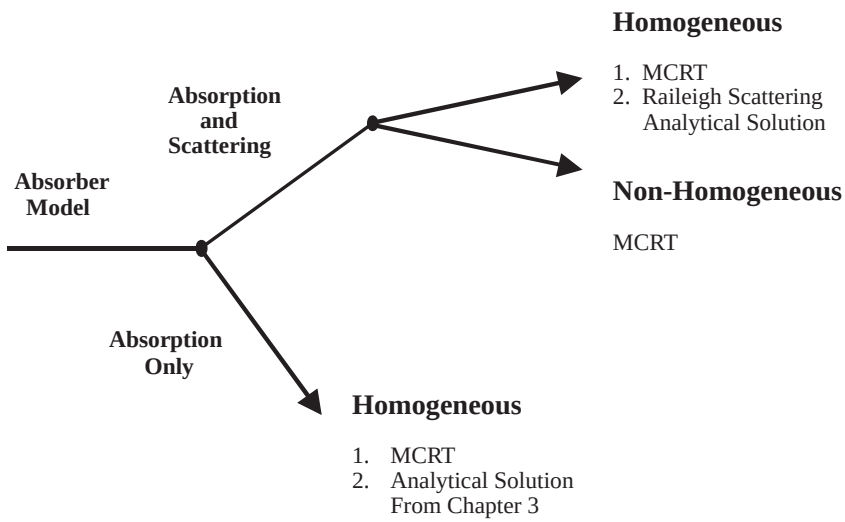

Figure 4.2: Different levels of models of the absorber.

4.2 Scattering in the Monte Carlo Method

Chemglaze is made up of finely divided carbon particles suspended in clear binder. Therefore, it is very likely that scattering should be taken into consideration. However, for simplicity, and since the model in Chapter 3 does not include scattering, scattering is not considered in this analysis. Figure 4.2 summarizes various ways in which the absorber layer can be modeled.

4.3 Absorption in the Monte Carlo Ray-Trace Method

Calculation of the absorption length requires knowledge of the band-averaged spectral absorption coefficient, $\overline{\kappa}_\lambda(\lambda)$, where λ is the centered wavelength of a finite $\Delta\lambda$ band. This coefficient, which has units of inverse length, is different from the extinction coefficient, κ, introduced earlier although they are related.

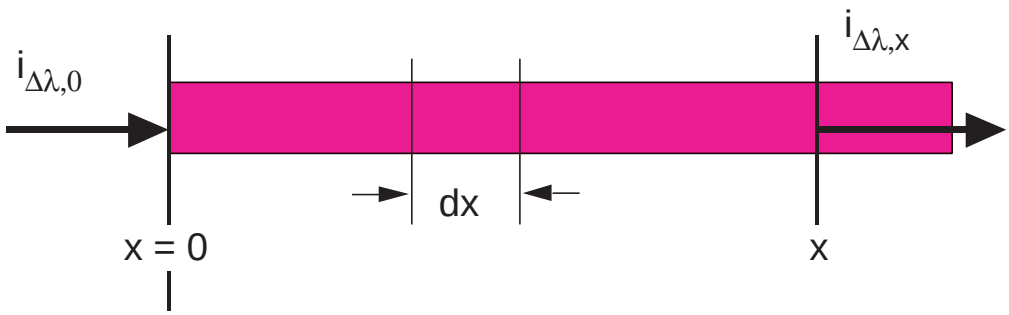

Figure 4.3: Attenuation of intensity through an absorbing medium.

We begin with the band-averaged version of Beer's law for an isotropic medium,

$$di_\lambda(\lambda, \mathbf{x}) \cong i_\lambda(\lambda, \mathbf{x} + d\mathbf{x}) - i_\lambda(\lambda, \mathbf{x}) \cong -\overline{\kappa}_\lambda(\lambda) i_\lambda(\lambda, \mathbf{x}) \ , \tag{4.1}$$

where i_λ is the spectral intensity defined in Chapter 2.

Integrating Equation 4.1 we get

$$\ell n | i_\lambda(\lambda, \mathbf{s}) |_{i_0}^{i_1} = -\overline{\kappa}_\lambda(\lambda)(x_1 - x_0) \ , \tag{4.2}$$

assuming that $\overline{\kappa}(\lambda)$ is uniform over the interval from x_0 to x_1. From the development in Chapter 3 it is clear that $i_\lambda(\lambda, \mathbf{x}) = \|\tilde{S}_{avg}\| / \Delta\lambda\omega$ where the relationship between the magnitude of the Poynting vector and the electric field strength was established earlier by Equation 3.7. Therefore, Equation 4.2 may be rewritten as

$$\frac{\|\tilde{E}_1^2\|}{\|\tilde{E}_0^2\|} = e^{-\overline{\kappa}_\lambda(\lambda)(x_1 - x_0)} \ . \tag{4.3}$$

Using Equation 3.37, Equation 4.3 can be simplified to

$$\overline{\kappa}_\lambda(\lambda) = \frac{4\pi\kappa}{\lambda} \ , \tag{4.4}$$

where $\overline{\kappa}$ is the band-averaged spectral absorption coefficient defined by Equation 4.1 and κ is the extinction coefficient defined by Equation 2.18.

The band-averaged spectral absorbance a_λ associated with a path length s_a is defined as

$$a_\lambda(s_a) = 1 - e^{-\overline{\kappa}_\lambda(\lambda)s_a} \ . \tag{4.5}$$

The band-averaged spectral absorptance can be interpreted as the probability that an energy bundle in wavelength $\Delta\lambda$ will be absorbed after it has traveled a distance s_a [Mahan, 2000]. Therefore, the next available random number, R_a can be set equal to the band-averaged spectral absorptance yielding

$$s_a = \frac{-1}{\overline{\kappa}_{ik}(\lambda)} ln(1 - R_a) \ , \tag{4.6}$$

where the subscript k is the index of the wavelength bands and the subscript i is the index of the volume element. In Equation 4.6 it is assumed that the random number is uniformly distributed between zero and unity.

All the rays are launched from Bin 0. The absorption length of each launched ray is given by Equation 4.6. The MCRT code must determine to which bin the absorption length corresponds. In addition, the MCRT code keeps track of the number of rays that are absorbed in each bin. This allows us to calculate the "numerical" heat generation function.

4.4 The Distribution Factor

The band-averaged spectral radiation distribution factor is defined as the "fraction of power emitted in wavelength interval $\Delta\lambda_k$ by surface element i that is absorbed by surface element j, both directly and due to all possible reflections within the enclosure" [Mahan, 2000].

The band-averaged spectral distribution factor can be approximated by

$$D_{ijk} \cong \frac{N_{ijk}}{N_{ik}} \ , \tag{4.7}$$

where N_{ik} is the number of energy bundles emitted from surface element i in wavelength band k, and N_{ijk} is the number of energy bundles absorbed by surface j.

Conservation of energy requires that

$$\sum_{k=1}^{m} \sum_{i=1}^{n} D_{ijk} = 1 \ , 1 \leq i \leq n \ ; \tag{4.8}$$

that is, all of the emitted energy bundles must be absorbed somewhere.

4.5 Orphan Rays

We now consider what happens when a ray has reflected from the bottom boundary of bin 10 and traveled back through bin 1 without being absorbed? Such unabsorbed rays are referred to as "orphan rays", because they belong to no bin. Mathematically orphan rays can occur in this model if the next available random number is close to unity, leading to an absorption length that is greater than twice the thickness of the absorber layer. The number of orphan rays will be few compared with the total number of rays launched. As a consequence, the best way to deal with them is to ignore them in the numerator or denominator of Equation 4.8. This ensures that their existence will have a negligible impact on the distribution factor calculation [Mahan, 2000].

4.6 Chapter Summary

This chapter introduces the Monte Carlo ray-trace method in participating media, an alternate method in predicting the absorption of radiation to that developed in the previous chapter. This chapter emphasizes four important parameters in this technique: the absorption length, scattering, the distribution factor, and orphan rays. Chapter 5 presents and compares the results using the analytical method derived in Chapter 3 and the probabilistic MCRT method.

Chapter 5

Results and Discussion

This chapter presents the results for the theory and models developed in Chapter 3 and Chapter 4. Section 5.1 constitutes a study of the convergence of the analytical heat generation model. Next, Section 5.2 develops the theory of the absorption of an EM wave in a conducting medium and describes the corresponding volumetric heat generation. This allows a volumetric heat generation term to be included in a finite difference code in order to compare the thermal response of the absorber layer with that predicted by a model assuming a surface boundary condition. This is the subject of Section 5.3. Section 5.4 presents the results of the reflectivity model. In the final section of the chapter, the heat generation function derived analytically for normal incidence from Maxwell's equations is compared with the volumetric heat generation distribution predicted using the MCRT method.

5.1 Convergence Results

The power flux contained by Wien's blackbody radiation distribution function is computed for a finite wavelength band. However, the power flux carried by the Poynting vector is for a specific wavelength. To reconcile this difference, we divide the Wien's function into wavelength intervals having width $\Delta\lambda$, with a finite $\Delta\lambda$ as shown in Figure 3.6. We then integrate the Wien's function over this finite wavelength interval and attribute the resulting power flux to that of a Poynting vector at the central wavelength of the interval. If the wavelength interval is sufficiently narrow, this is in an adequate approximation. The total power flux is then the sum of that due to a finite number of discrete Poynting vectors.

The question now becomes, how small does the finite $\Delta\lambda$ band need to be? To answer this question, a convergence study was done to see at what values of $\Delta\lambda$ the heat generation converges. The convergence study began a with a $\Delta\lambda$ of 1 μm. As it can be seen on Table 5.1, the heat generation converges for a band of $\Delta\lambda$ of 1/35 or 0.029 μm.

5.2 Volumetric Heat Generation due to an Electromagnetic Wave at Normal Incidence

5.2.1 Electric Fields in Semi-Infinite Thin Films

Numerical experiments were performed to find the electrical resistivity using the optical properties given Figure 2.8. The electrical resistivity was found by trial-and-error using the criterion that the correct value must satisfy conservation of energy. Since electrical resistivity is not wavelength dependent, this value could be determined at any wavelength and then

Table 5.1: For depths of 1, 5, and 10 μm into a semi-infinite absorber layer (λ = 10 μm, $\Delta\lambda$ = 1, r_e = 0.0001 Ω·m, κ = 0.8, n = 1.55).

Number of Subintervals	$\dot{g}$(1 μm) (W/m^3)	$\dot{g}$(5 μm) (W/m^3)	$\dot{g}$(10 μm) (W/m^3)
1	8.69184×10^6	155851	1022.60
5	8.69289×10^6	157203	1061.11
10	8.69293×10^6	157245	1062.32
15	8.69293×10^6	157253	1062.54
20	8.69294×10^6	157256	1062.62
25	8.69294×10^6	157257	1062.66
30	8.69294×10^6	157258	1062.68
35	8.69294×10^6	157258	1062.69
50	8.69294×10^6	157259	1062.70

used at other wavelengths to verify if energy was conserved at these other wavelengths. Table 5.2 shows the results of the numerical experiments. The optical constants in Figure 2.8 were approximated using the following fits:

$$n(\lambda) = 1.2e^{0.0017\lambda} \tag{5.1}$$

and

$$\kappa(\lambda) = \frac{-0.5}{120}\left(\frac{10000}{\lambda}\right) + \frac{4}{3}\,. \tag{5.2}$$

The percent error in the conservation of energy requirement is defined as

$$\%Error = \frac{q_{E_t} - q_{Absorber}}{q_{E_t}} \times 100\,, \tag{5.3}$$

where q_{E_t} is the heat flux carried by transmitted electromagnetic wave and $q_{Absorber}$ is $\int_{x_0}^{L} \dot{g}(x, T_{EARTH})dx$ in the interested wavelength interval as demonstrated by Equation 3.46.

Table 5.2: Results of the numerical experiments to determine the electrical resistivity of the carbon-black loaded binder from the optical constants shown in Figure 2.8.($\Delta\lambda$ = 0.029 μm, absorber length = 100 μm) .

Wavelength Interval	Electrical Resistivity (Ω·m)	Error in Conservation of Energy
100-101 μm	0.00210	-0.16%
75-76 μm	0.00227	0.95%
50-51 μm	0.00209	-0.24%

In order to model the behavior of the absorber at lower wavelengths, the Hagen-Rubens theory, introduced in Section 2.5, was used. In other words, in what follows we assume that n = κ at all wavelengths within the absorber layer. This is done with the knowledge (a) that carbon is not a metal and (b) that even metals at long wavelengths, n and κ may differ by several hundred percent as shown in Table 2.2.

5.2.2 Internal Heat Generation Due to Near Infrared Radiation

Figure 5.1 shows the attenuation of the real and imaginary parts of in a 10-μm EM wave propagating through a semi-infinite absorber with r_e = 0.00025 Ω·m, where n and κ are computed using Equation 2.21. As the wave propagates, the relative phase angle constantly changes as shown in Figure 5.3. Figure 5.2 shows the corresponding exponential decay in the magnitude of the electric field intensity, and the corresponding volumetric heat generation due to this absorption is shown by Figure 5.4.

The heat generation can also be obtained for any arbitrary finite wavelength interval, as can be seen in Figure 5.5. Figure 5.5 shows the heat generation due to radiation in the

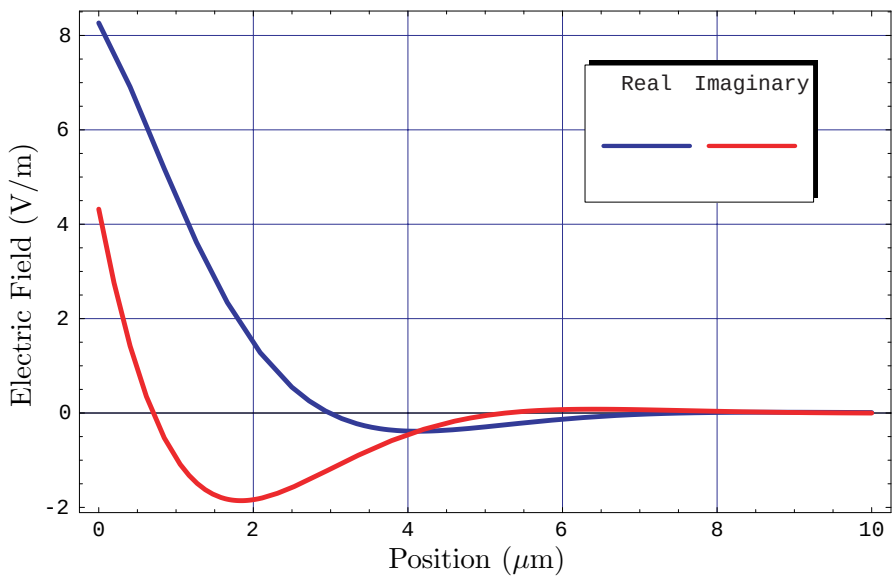

Figure 5.1: Real and imaginary components of incident 255-K blackbody radiation for a 10.5-μm wave with a $\Delta\lambda = 0.029$ μm ($r_e = 0.00025$ Ω·m).

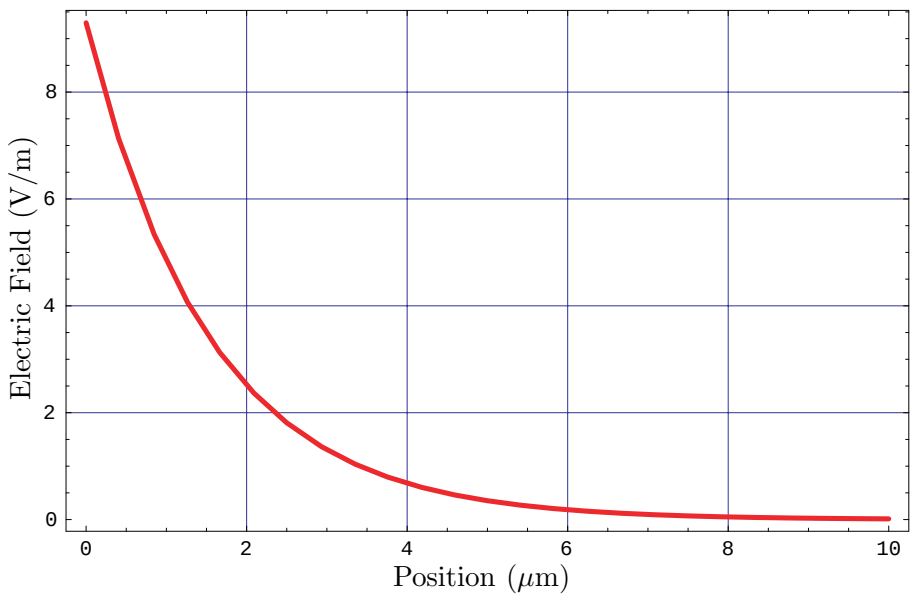

Figure 5.2: Absorption of incident 255-K blackbody radiation for a 10.5-μm wave with $\Delta\lambda$ = 0.029 μm in a medium (r_e = 0.00025 Ω·m).

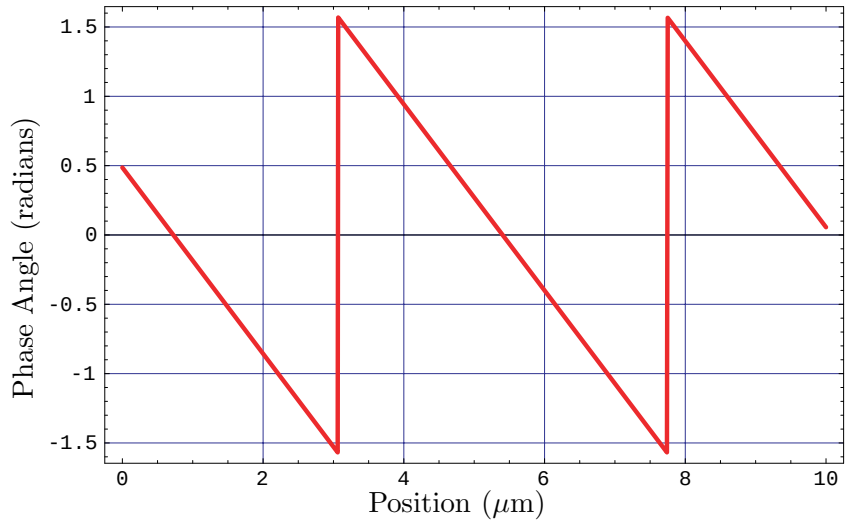

Figure 5.3: Change in phase angle of incident 255-K blackbody radiation for a 10.5-μm wave with $\Delta\lambda = 0.029$ μm in a medium ($r_e = 0.00025$ Ω·m).

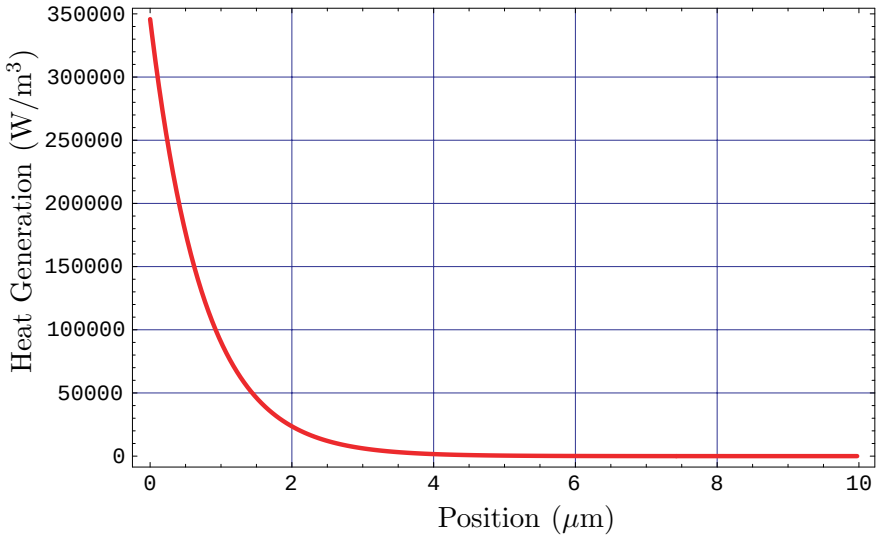

Figure 5.4: Heat generation due incident 255-K blackbody radiation for a wavelength of 10.5 μm with a $\Delta\lambda = 0.029$ μm ($r_e = 0.00025$ Ω·m) .

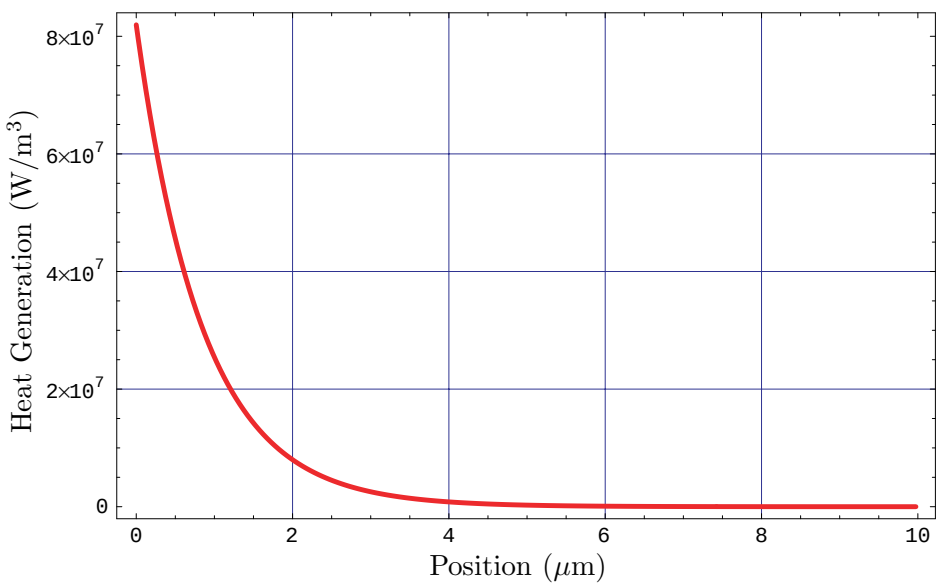

Figure 5.5: Heat generation due to incident 255-K blackbody radiation in the wavelength interval between 10 and 19.97 μm waves (r_e = 0.00025 Ω·m) .

wavelength interval from 10 to 19.97 μm. The radiant heat flux is obtained by integrating the heat generation through the depth of the absorber. The corresponding flux is given by

$$q = \int_0^L \sum_{\lambda=\lambda_{min}}^{\lambda_{max}} \dot{g}(x, \lambda, \Delta\lambda = \frac{1}{35}, T_{EARTH})dx \ . \tag{5.4}$$

where L = 10 μm and for the case at hand λ_{min} is 10 and λ_{max} is 19.97 μm. With these parameters Equation 5.4 results in a heat flux of 70.31 W/m^2, which is excellent agreement with the power carried by the transmitted electromagnetic wave, 70.12 W/m^2.

5.2.3 Heat Generation Due to Far Infrared Radiation

Figures 5.6 and Figures 5.7 show the heat generation for the same resistivity with a wavelengths of 50.5 and 50-74.97 μm respectively, which is in the far infrared region. It can be seen that the heat generation due to longer wavelengths is much lower than near infrared region. This is expected since the peak of the blackbody radiation distribution function is about 10 μm (See Figure 2.1). Also, it can be seen less energy is absorbed at the surface for the longer wavelengths.

5.2.4 Restrictions of the Models

The lack of knowledge of properties such as the permittivity and the electrical resistivity of Chemglaze encouraged us to rely in the Hagen-Rubens theory to test the model. The conditions of the Hagen-Rubens approximation were mentioned in Chapter 2. An implicit restriction of this theory is the real part of the complex index of refraction, n, must by definition be greater or equal to unity. Therefore, the results presented here are limited to cases for which the index of extinction is also greater than or equal to unity. It should be

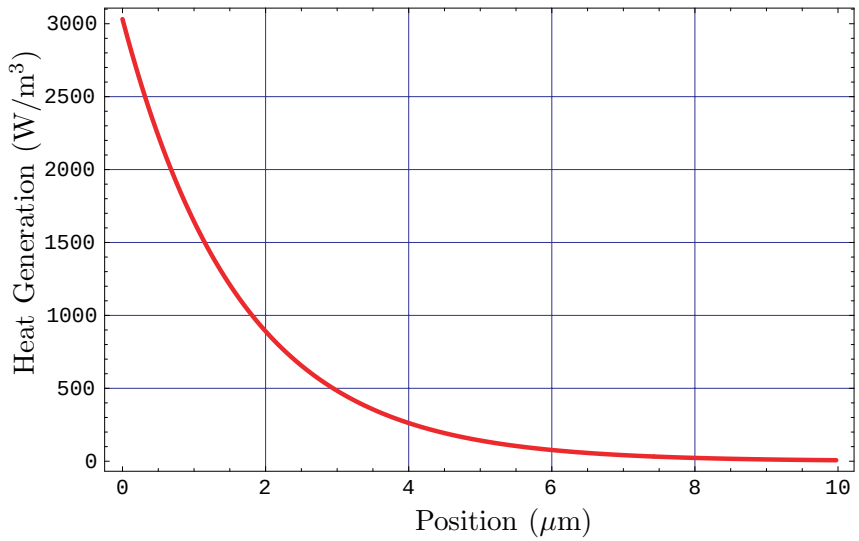

Figure 5.6: Heat generation due to 255-K blackbody radiation for a wavelength of 50.5 μm (r_e = 0.00025 Ω·m).

mentioned that using the Hagen-Rubens approximation in the analytical model works well for low electrical resistivities (i.e. n < 1).

As in the case of other finite difference schemes, the current model presents opportunities for obtaining erroneous results. These include using inadequate spatial or spectral resolution and using an overly thick absorber or too high of a resistivity. The high electrical resistivity will ensure that most of the radiation is absorbed in the outer-most layer, while excessive depth of the absorber will reduce the spatial resolution of the scheme.

If the index of extinction is very low, then none of the models presented in Chapter 3 are valid unless the absorber is deep. The reason for this is that it takes several reflections back and forth with in the absorber layer for a significant amount of the energy in the wave to be absorbed.

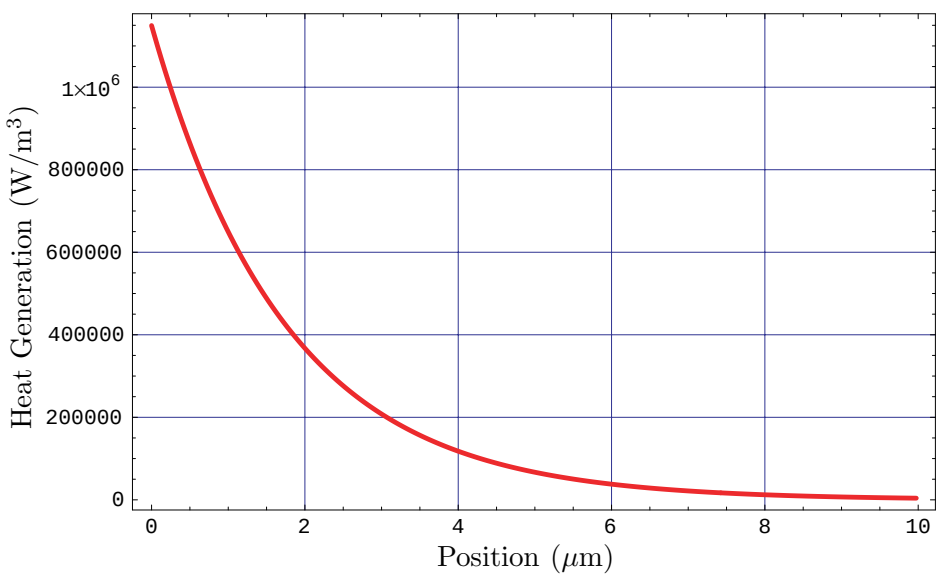

Figure 5.7: Heat generation due to incident 255-K blackbody radiation in the wavelength interval between 50 and 74.97 μm (r_e = 0.00025 Ω·m) .

5.3 Temperature Distribution Through the Multi-Layer Detector

A one-dimensional finite difference code originally written for a graduate-level conduction class was employed to determine the transient and steady state thermal behavior of the detector. This code does not take into consideration the effect of contact resistance between the layers. The contact resistance between layers is probably important, but at this time its value is unknown. More information on the effect of contact resistance in this detector may be found in Barry [1999].

5.3.1 Temperature Response Due to Near Infrared Radiation

The steady temperature distribution is shown by Figures 5.8 and 5.9, respectively, for the case of the surface absorption model and the volumetric heat generation in the wavelength interval between 10 and 19.97 μm. Figures 5.8 and 5.9 seem identical. This is expected because the energy entered into each model was the same and in the heat generation model most of the radiation was absorbed near the surface. Also, one can see, that these figures are essentially a scaled version (70 times) of Figure 4 from Barry [1999]. Figure 5.10 shows that the model with absorption surface gives a slightly faster temperature rise than the model with the volumetric heat generation. Figure 5.11 shows the temperature response of the active junction to be practically identical in both models.

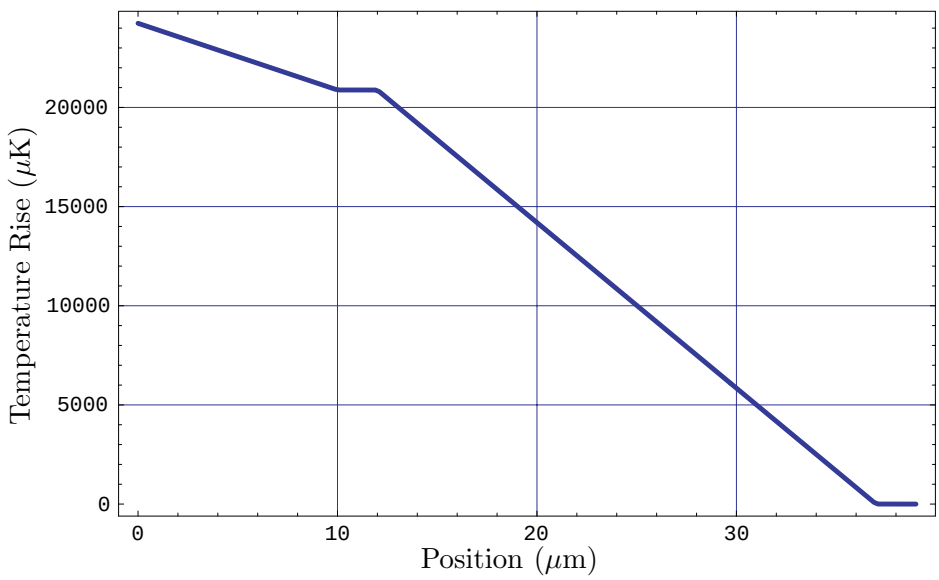

Figure 5.8: Steady-state temperature distribution of detector using the surface absorption model in the wavelength interval between 10 and 19.97 μm waves.

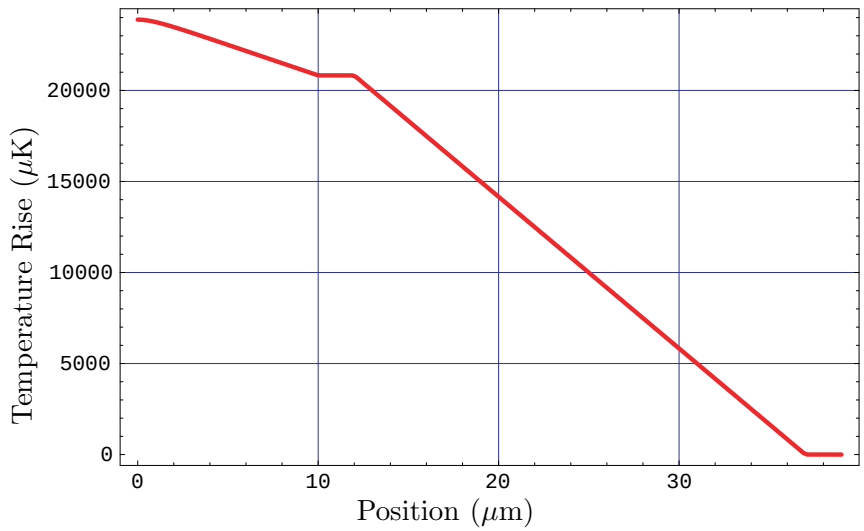

Figure 5.9: Steady-state temperature distribution through the detector according to the volumetric heating model in the wavelength interval between 10 and 19.97 μm waves.

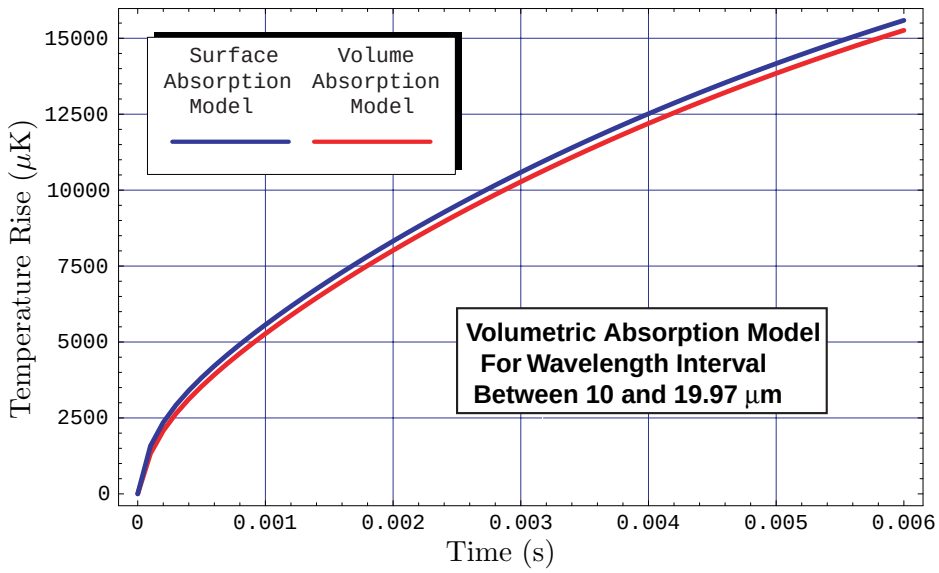

Figure 5.10: Temperature response of the upper surface of the detector (x = 0) for the surface absorption model and the volumetric absorption model in the near-infrared.

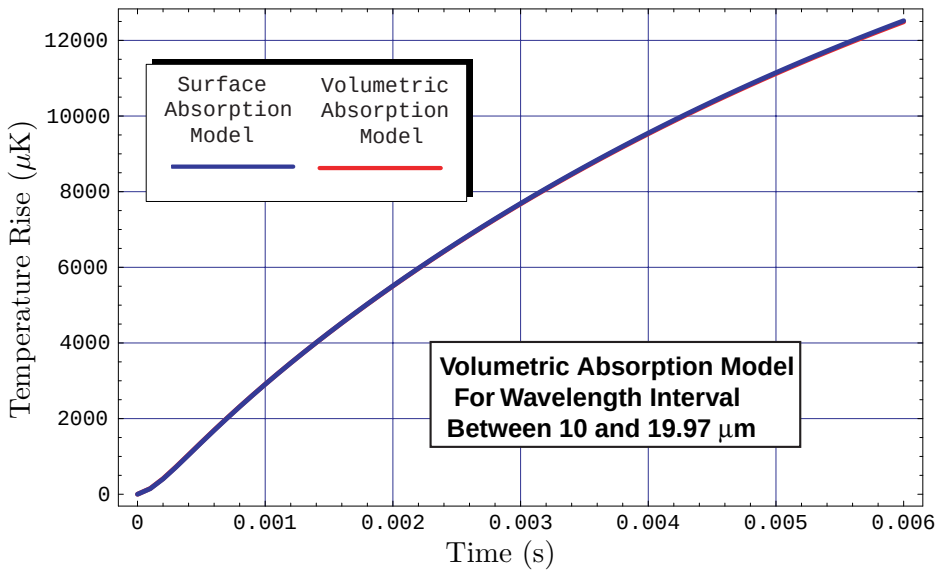

Figure 5.11: Temperature response of active junction (x = 11 μm) for the surface absorption model and the volume absorption model in the near-infrared.

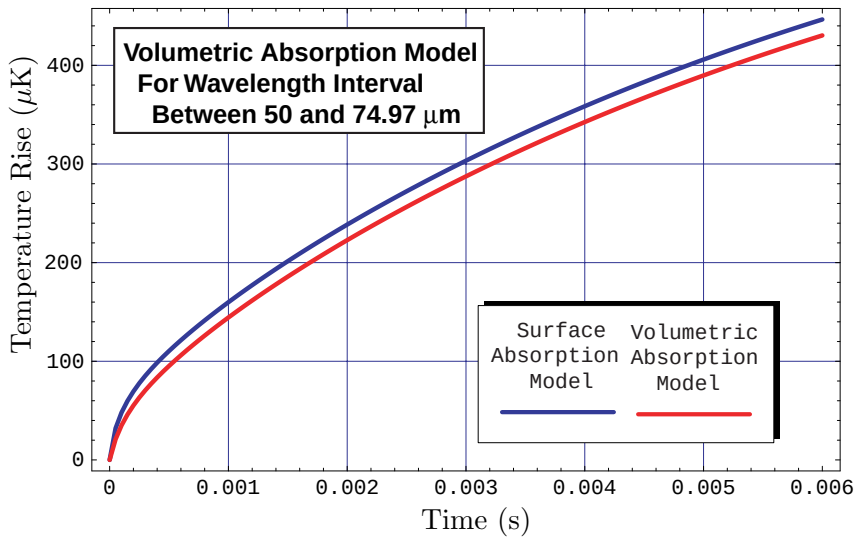

Figure 5.12: Temperature response of the upper surface of the detector (x = 0) for the surface absorption model and the volumetric absorption model in the far-infrared.

5.3.2 Temperature Response Due to Far Infrared Radiation

The temperature response of the detector due to incident radiation in the far infrared is identical to that due to the in the near infrared. Whether the detector is modeled with a constant surface absorption or with a volumetric heat generation in the absorber layer does not make much difference as illustrated by Figures 5.12 and 5.13. However, a slight difference can be seen by comparing the response in Figure 5.12 with that in Figure 5.10; the difference between the surface flux model and the volumetric absorption model is greater in the far infrared than in the near infrared. This can be attributed to the fact that radiation requires a greater depth to be absorbed at long wavelengths than at shorter wavelengths, and so deviates more from the surface flux model.

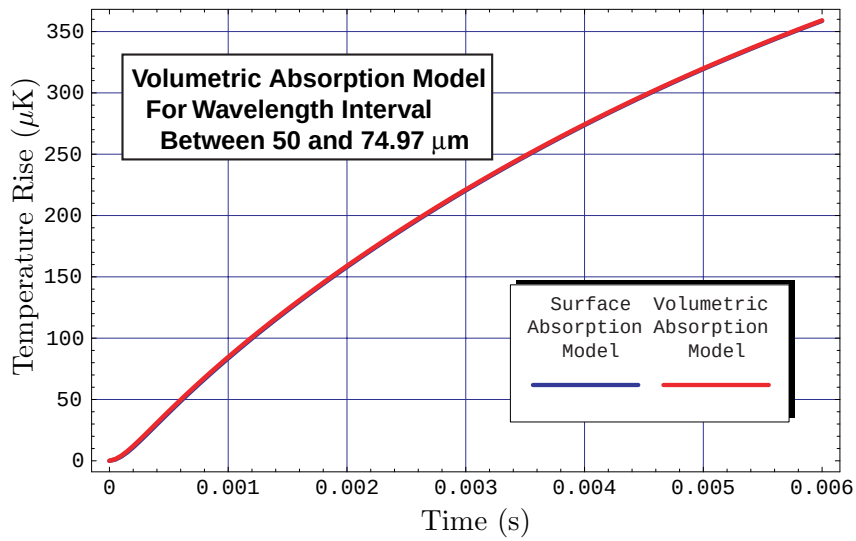

Figure 5.13: Temperature response of active junction (x = 11 μm) for the surface absorption model and the volume absorption model in the far-infrared.

5.4 Reflection from the Absorber Layer

Reflectivity data available from the literature for a black absorber are limited to the far-infrared region, as illustrated by Figure 5.14. The data shown are for absorber layers with a thickness of 40 μm on top of a gold-coated glass mirror assumed to have a one-hundred percent reflectivity. The data indicate a strong interference effect between the rays that reflect immediately from the absorber layer and those that reflect from the second surface-mirror.

Blue and Perkowitz [1992] and Smith [1984] used models similar to the one described in Chapter 3 to fit the reflectivity data and back out the optical constants. Using a fitting routine from the International Mathematics and Science Library, Inc., Smith [1984] calculated an index of refraction of 1.37 and an index of extinction of 0.066 for the prelaunch reflectance of a black absorber layer similar to those under the study in this thesis. Blue and Perkowitz

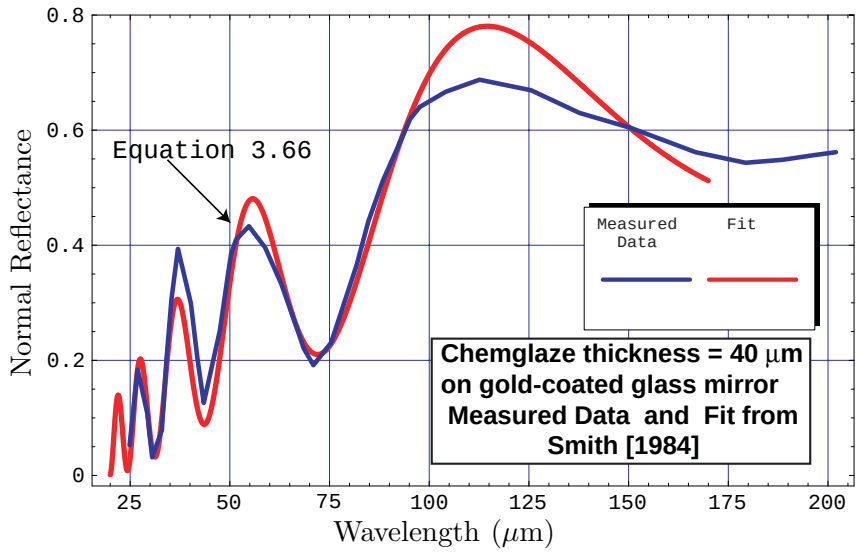

Figure 5.14: Smith [1984] fit of measured reflection data for Chemglaze (Data are at 17° incidence).

[1992] also calculated the same index of refraction, but a slightly larger index of extinction, 0.22, for Chemglaze after five years spent in near-earth orbit. The model fit in Figure 5.14 follow the data extremely well. However, these fitting models do not take into account the variation in index of refraction with wavelength predicted by Equations 2.17 and 2.18.

The Hagen-Rubens approximation cannot reasonably be used to estimate these optical constants since the n and κ are not in the same order of magnitude. In the present effort, the optical constants are approximated using a semi-empirical method. The real index of refraction is estimated as an exponentially decreasing function, as suggested by data in Figure 2.8. The fit used for n is given by Equation 5.1. The fit for κ is based on the Hagen-Rubens approximation. An electrical resistivity of 0.516 Ω·m is used to obtain an extinction coefficient of 0.066 at 75 μm. The resulting semi-empirical fit shown in Figure 5.14 does not reproduce the measured data as well as the purely empirical fit used by Smith; however it reproduces

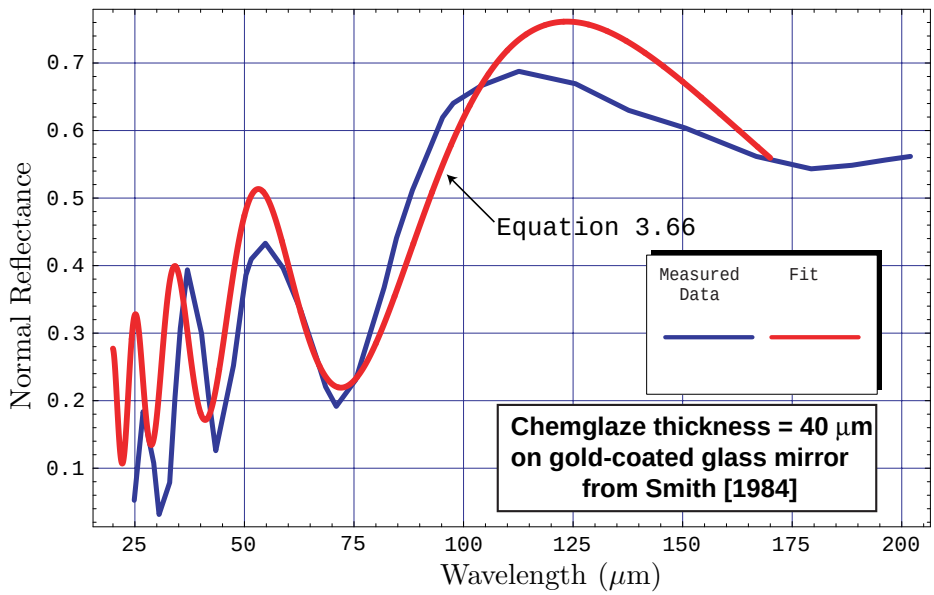

Figure 5.15: Semi-empirical fit of measured reflection data for Chemglaze (Data are for 17° incidence).

the trend in the data about as well. Even though the reflection model predicts the measured data reasonably well, it must be noted that the absorber has to be much greater than 80 μm to only consider the first two terms of the reflection model. This is because the extinction coefficient used, 0.066, ensures that the EM wave has a significant amount of energy after reflecting from the second-surface mirror and reaching the top of the absorber. Since Smith [1984] only considered the first two terms of the reflection model, the extinction coefficient he estimated may be not accurate.

5.5 Monte Carlo Ray-Trace Model for Volumetric Heat Generation

A MCRT analysis was performed on the detector in which up to 2 million rays were traced. This allows an independent validation of the radiation absorption results obtained using the models described in Chapter 3. To facilitate the comparison, "analytical" band-averaged distribution factors were calculated for a centered wavelengths of 10.5 and 50.5 μm, with $\Delta\lambda$ = 0.029 μm . The analytical band-averaged distribution factors were calculated numerically using

$$D_{0jk,analytical} = \frac{\int_{x_j}^{x_j+\Delta x} \dot{g}(x, \lambda_k, \Delta\lambda_k, T)dx}{\int_0^{\ell} \dot{g}(x, \lambda_k, \Delta\lambda_k, T)dx} \ . \tag{5.5}$$

The MCRT analysis essentially converged after about 500,000 rays have been traced. However, it can be seen by referring to Figure 5.16 that with only 1000 rays the distribution factors are different from their converged values by less than one percent. Figures 5.17 and 5.18 illustrate the distribution of absorbed rays are absorbed in the absorber layer at two different wavelengths. These figures resemble Figures 5.4 and 5.6, and upon close inspection they are in fact the identical. This is evident by comparing the statistical distribution factors, given in Table 5.4, obtained from the MCRT analysis and the analytical distribution factors computed using Equation 5.5.

5.6 Chapter Summary

This chapter presents the results from theory derived in Chapters 3 and 4. It establishes a value for which a band of width $\Delta\lambda$ represents radiation at wavelength centered at λ. Next it is demonstrated how EM waves are absorbed in films and how this absorbed heat

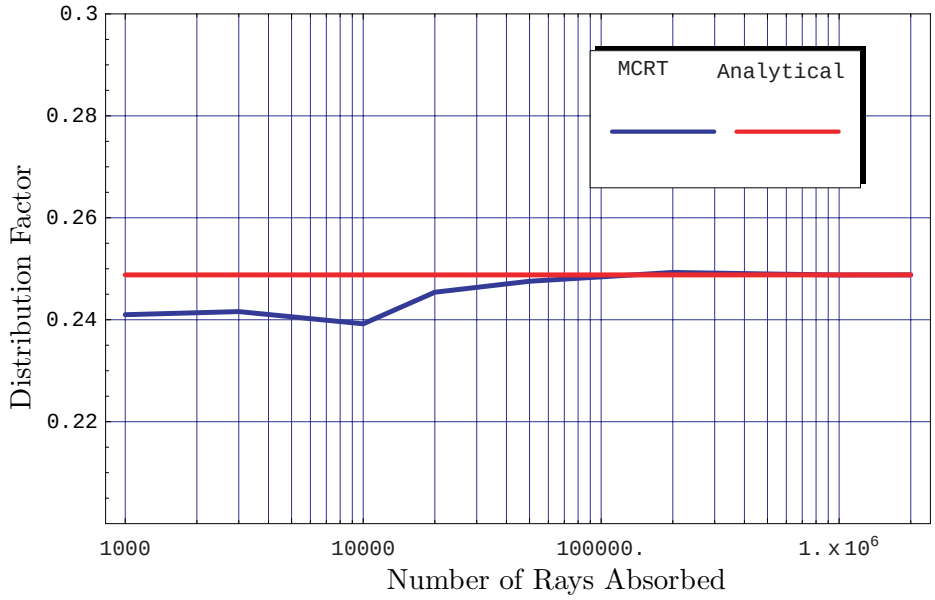

Figure 5.16: Convergence of the distribution factor $D_{0,2}$ for a band with central wavelength of 50.5 μm and bandwidth is 0.029 μm.

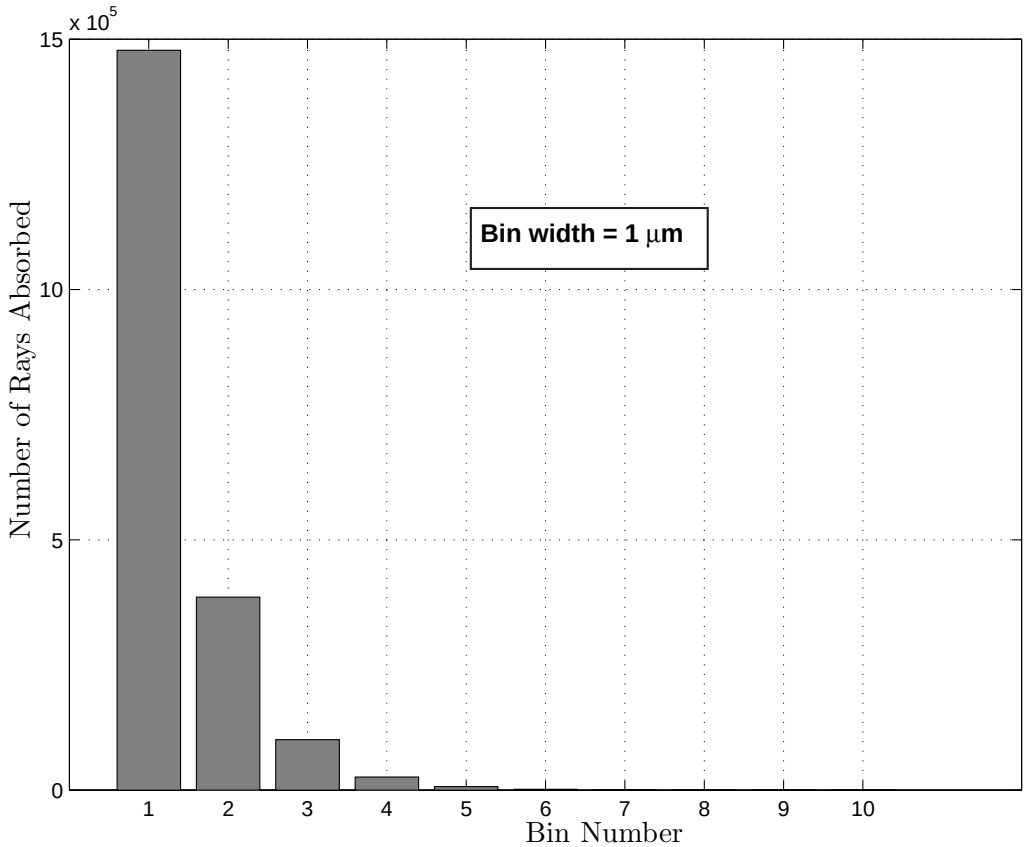

Figure 5.17: Distribution of absorbed energy bundles by bin number for a band with central wavelength of 10.5 μm and width is 0.029 μm (r_e=0.00025 Ω·m).

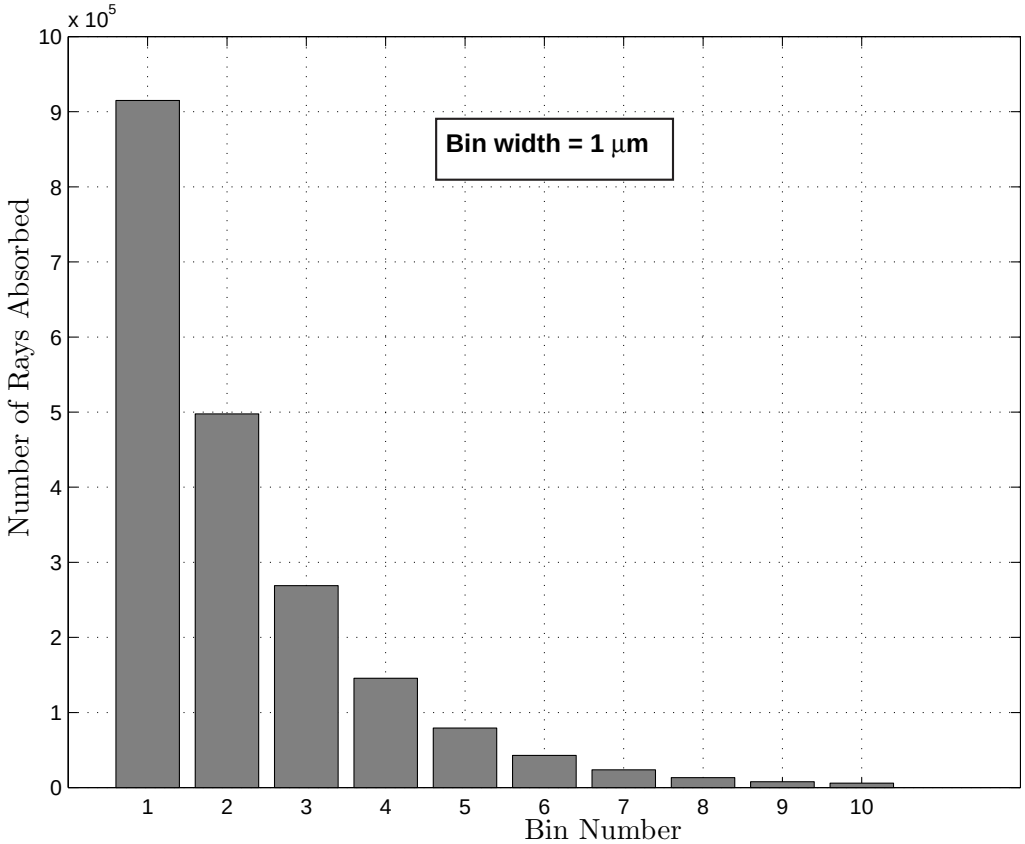

Figure 5.18: Distribution of absorbed energy bundles by bin number for a band with central wavelength of 50.5 μm and width is 0.029 μm (r_e=0.00025 Ω·m).

Table 5.3: Analytical and statistical band-averaged distribution factors for a bands with a central wavelength of 10.5 and bandwidth is 0.029 μm (r_e=0.00025 Ω·m).

Bin Number	Analytical Distribution Factor (D_{0jk})	Statistical Distribution Factor (D_{ijk})
1	0.7389	0.7389
2	0.1929	0.1928
3	0.0504	0.0503
4	0.0132	0.0132
5	0.0034	0.0034
6	0.0009	0.0008
7	0.0002	0.0002
8	6.11×10^{-5}	5.75×10^{-5}
9	1.54×10^{-5}	2.24×10^{-5}
10	3.99×10^{-6}	6.49×10^{-6}

absorption leads to heat generation. This chapter also presents reflectivity data for absorber materials and illustrates the shortcomings of proposed reflection models. Finally, using a different technique, the MCRT method produces results that agree with the results obtained analytically by solving Maxwell's equations.

Table 5.4: Analytical and statistical band-averaged distribution factors for a bands with a central wavelength of 50.5 and bandwidth of 0.029 μm (r_e=0.00025 Ω·m).

Bin Number	Analytical Distribution Factor (D_{0jk})	Statistical Distribution Factor (D_{0jk})
1	0.4589	0.4574
2	0.2488	0.2488
3	0.1348	0.1344
4	0.07311	0.0728
5	0.0396	0.0397
6	0.0215	0.0214
7	0.0116	0.0118
8	0.0063	0.0066
9	0.0034	0.0039
10	0.0018	0.002913

Chapter 6

Conclusion and Recommendations

The primary goals of this research were to study the absorption and reflection of radiation in thin-film absorber layers. The behavior of absorption was studied using three absorption models: a surface absorption model, an analytical volumetric absorption model, and a numerical volumetric model. The reflection model takes into consideration the second-surface mirror configuration of the detector. The reflection model accounts the immediate reflection of the absorber layer and the first reflection from the second-surface mirror.

6.1 Conclusions

The following conclusions can be drawn about radiation absorption in a thin-film absorber based on the analysis on this thesis:

1. The absorption and reflection of electromagnetic radiation in a second-surface mirror thin film can be modeled on the basis of electromagnectic theory and optics.

2. The heat generation model verifies that the nonuniform heat generation in the absorber layer can be treated as a surface heat flux condition if the extinction coefficient is sufficiently large or if the layer is sufficiently thick compared with the wavelength of the incident radiation. The analysis presented indicates that volumetric absorption results in a lower temperature at the surface than for a surface heat flux.

3. The reflection model explains why if the extinction coefficient is sufficiently small, interference has a strong influence on the spectral distrubution of reflectivity.

4. A MRCT-based model produces results that agree very well with the results obtained with the analytical volumetric heat generation model.

6.2 Recommendations

The effort and results reported in this thesis suggest several avenues for further research:

1. A campaign to meausure the reflectivity of absorber thin-film layers in the visible and near-infrared regions should be undertaken.

2. The reflectivity data obtained in a dedicated experimental campaign should be used to recover, using suitable parameter estimation methods the extinction coefficient and index of refraction.

3. A model should be develped that accounts for more reflections and volumetric scattering within the absorber layer.

References

Barry, M., 1999, **Heat Transfer Issues in Thin-Films**, M.S. Thesis, Virginia Polytechnic Institute and State University.

Blue, M. and Perkowitz, S., 1992, *Space-Exposure Effects on Optical-Baffle Coatings at Far-Infrared Wavelengths*, **Applied Optics**, Vol. 31, No. 21, pp. 4305–4309.

Blythe, A., 1979, **Electrical Properties of Polymers**, Cambridge University Press.

Bordi, F., Neeck, S., and Scolese, C., 1997, EOS AM: Progress, Plans, and Promise, http://eos-am.gsfc.nasa.gov/presentations/torino.pdf.

Calahorra, A., 1988, *Investigation of Electrical Resistivity-Pigment Volume Concentration Relationship in Carbon Black Filled Conductive Paint*, **Journal of Coatings Technology**, Vol. 60, No. 757, pp. 25–30.

Cheng, D., 1992, **Field and Wave Electromagnetics**, Addison-Wesley.

Grammer, J., Bailin, L., Blue, M., and Perkowitz, S., 1980, *Absorbing Coatings for the Far Infrared*, **Proceedings of SPIE**, Vol. 257, No. 3, pp. 192–195.

Hagen, E. and Rubens, H., 1900, *Metallic Reflection*, **Ann. Physics**, Vol. 1, No. 2, pp. 352–375.

Hecht, E. and Zajac, A., 1974, **Optics**, Addison-Wesley.

Lee, R. B., Gibson, M., Wilson, R., and Thomas, S., 1995, *Long-Term Total Solar Irradiance Variability During Sunspot Cycle 22*, **Journal of Geophysical Research A**, Vol. 100, No. 2, pp. 1667–1675.

Lide, D. R., 1998, **Handbook of Chemistry and Physics**, CRC Press.

Mahan, J., 2000, **Radiation Heat Transfer**, Manuscript.

NASA, 2000, Tropical Rainforest Measurement Mission, http://trmm.gsfc.nasa.gov/.

Ramanathan, V., Barkstrom, B., and Harrison, E., 1989, *Climate and the Earth's Radiation Budget*, **Physics Today**, Vol. 8, No. 4, pp. 22–32.

Sánchez, M., 1998, **Optical Analysis of a Linear-Array Thermal Radiation Detector for Geostationary Earth Radiation Budget Applications**, M.S. Thesis, Virginia Polytechnic Institute and State University.

Seigel, R. and Howell, J., 1992, **Thermal Radiation Heat Transfer**, Hemisphere Publishing Corp.

Smith, S., 1984, *Specular Reflectance of Optical-Black Coatings in the Far Infrared*, **Applied Optics**, Vol. 23, No. 14, pp. 115–127.

Smith, S. and Howitt, R., 1986, *Survey of Material for an Infrared Opaque-Coating*, **Proceedings of SPIE**, Vol. 646, No. 3, pp. 96–103.

Sorensen, I. J., 1998, **Analytical and Experimental Characterization of a Linear-Array Thermopile Scanning Radiometer for Geo-Synchronous Earth Radiation Budget Applications**, M.S. Thesis, Virginia Polytechnic Institute and State University.

Weckmann, S., 1997, **Dynamic Electrothermal Model of a Sputtered Thermophyle Thermal Radiation Detector for Earth Radiation Budget Applications**, M.S. Thesis, Virginia Polytechnic Institute and State University.

Appendix A

Nomenclature for Operations Involving Harmonic Vector Quantities

Consider complex vector $\tilde{\mathbf{a}}$

$$\tilde{\mathbf{a}} = Re[\tilde{a}_x\mathbf{i} + \tilde{a}_y\mathbf{j} + \tilde{a}_z\mathbf{k}] + iIm[\tilde{a}_x\mathbf{i} + \tilde{a}_y\mathbf{j} + \tilde{a}_z\mathbf{k}] = \\ \{Re[\tilde{a}_x] + iIm[\tilde{a}_x]\}\mathbf{i} + \{Re[\tilde{a}_y] + iIm[\tilde{a}_y]\}\mathbf{j} + \{Re[\tilde{a}_z] + iIm[\tilde{a}_z]\}\mathbf{k}\ . \quad \text{(A.1)}$$

where Re denotes the real part of a complex number $\tilde{a}$, Im denotes the imaginary part number operator of a complex number $\tilde{a}$, $\mathbf{i}$, $\mathbf{j}$, $\mathbf{k}$ are respectively, the unit vectors in the x, y, and z direction, and i is the imaginary number operator, $\sqrt{-1}$.

Now consider the **i**-component only as shown in Figure A.1. In this case the magnitude and phase angle of $\tilde{\mathbf{a}}$ are

$$\|\tilde{a}_x\| = \sqrt{(Re[\tilde{a}_x])^2 + (Im[\tilde{a}_x])^2} \quad \text{(A.2)}$$

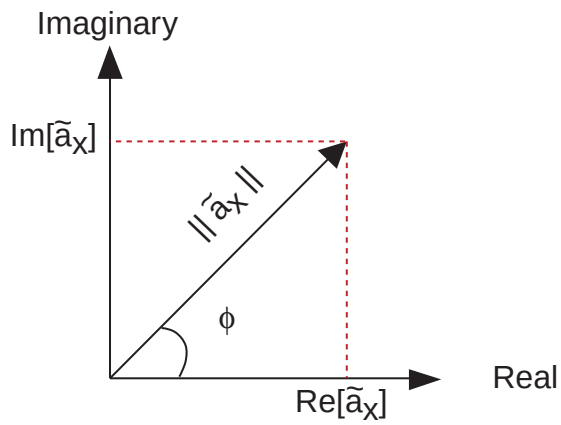

Figure A.1: The magnitude, phase angle and real and imaginary parts of a complex scalar.

and

$$\phi = \tan^{-1} \frac{Im[\tilde{a}_x]}{Re[\tilde{a}_x]} \ , \tag{A.3}$$

respectively.

Now considering all directions as shown in Figure A.2, vector $Re[\tilde{\mathbf{a}}]$ can be expressed

$$\tilde{\mathbf{a}} = \|\tilde{a}_x\|\mathbf{i} + \|\tilde{a}_y\|\mathbf{j} + \|\tilde{a}_z\|\mathbf{k} \ . \tag{A.4}$$

The magnitude of vector $\mathbf{a}$ is

$$|\ \|\tilde{\mathbf{a}}\|\ | = \sqrt{\|\tilde{a}_x\|^2 + \|\tilde{a}_y\|^2 + \|\tilde{a}_z\|^2} \ , \tag{A.5}$$

where

$$\|\tilde{a}_x\|^2 = \{Re[\tilde{a}_x] + Im[\tilde{a}_x]\}\{Re[\tilde{a}_x] + Im[\tilde{a}_x]\}^* \ . \tag{A.6}$$

Equation A.6 can be rewritten as

$$\|\tilde{a}_x\|^2 = \{Re[\tilde{a}_x] + Im[\tilde{a}_x]\}\{\Re[\tilde{a}_x] - Im[\tilde{a}_x]\} \ . \tag{A.7}$$

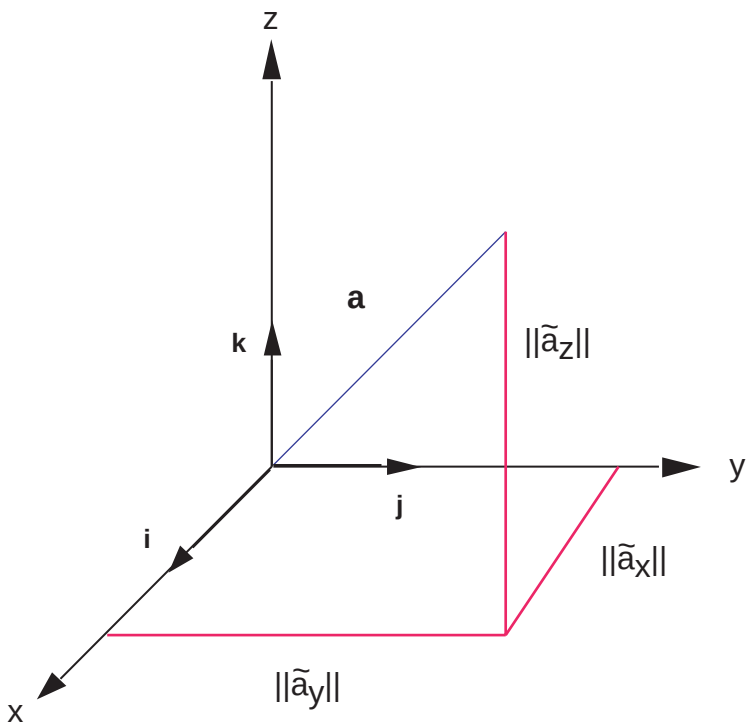

Figure A.2: A three-dimensional vector and its components .

Equation A.7 can be simplified to

$$\|\tilde{a}_x\|^2 = (Re[\tilde{a}_x])^2 + (Im[\tilde{a}_x])^2 \ . \tag{A.8}$$

likewise

$$\|\tilde{a}_y\|^2 = (Re[\tilde{a}_y])^2 + (Im[\tilde{a}_y])^2 \tag{A.9}$$

and

$$\|\tilde{a}_z\|^2 = (Re[\tilde{a}_z])^2 + (Im[\tilde{a}_z])^2 \ . \tag{A.10}$$

Consider the $\hat{\mathbf{i}}$-direction again

$$\tilde{\mathbf{a}} = (x + iz)\mathbf{i} \ . \tag{A.11}$$

The complex conjugate of $\tilde{\mathbf{a}}$ is

$$\tilde{\mathbf{a}}^* = (x - iz)\mathbf{i} \ . \tag{A.12}$$

$$\tilde{\mathbf{a}} \cdot \tilde{\mathbf{a}}^* = (x^2 + z^2) \ . \tag{A.13}$$

Consider the operation

$$\|\tilde{a}_x^2\| = \|(x + iz)(x + iz)\| \ . \tag{A.14}$$

the binomial

$$\|\tilde{a}_x^2\| = \|x^2 + 2xzi - z^2\| \ . \tag{A.15}$$

Rearranging terms

$$\|\tilde{a}_x^2\| = \|x^2 - z^2 + 2xzi\| \ , \tag{A.16}$$

which can be rewritten as

$$\|\tilde{a}_x^2\| = \sqrt{(x^2 - z^2)^2 + (2xz)^2} \ , \tag{A.17}$$

expanding both terms

$$\|\tilde{a}_x^2\| = \sqrt{x^4 + 2x^2z^2 + z^4} \ . \tag{A.18}$$

This can be simplified to

$$\|\tilde{a}_x^2\| = \sqrt{(x^2 + z^2)(x^2 + z^2)} \ , \tag{A.19}$$

and finally

$$\|\tilde{a}_x^2\| = (x^2 + z^2), \tag{A.20}$$

which is the same result from Equation A.13.

Now consider the following operation

$$\|\tilde{a}_x\|^2 = \|(x + iz)\|^2 \ . \tag{A.21}$$

Rewritting Equation A.21

$$\|\tilde{a}_x\|^2 = (\sqrt{x^2 + z^2})^2 \ , \tag{A.22}$$

which simplifies to

$$\|\tilde{a}_x\|^2 = x^2 + z^2 \ , \tag{A.23}$$

Therefore, it can be concluded that

$$\tilde{\mathbf{a}} \cdot \tilde{\mathbf{a}}^* = \|\tilde{a}_x\|^2 = \|\tilde{a}_x^2\| \ . \tag{A.24}$$

Appendix B

Derivation of Incident-Reflecting Heat Generation Function

Equation 3.37 can be rewritten as

$$E_{in,y}(x,\lambda,\Delta\lambda,T) = \frac{\tilde{E}_t(m-\Delta\lambda/2, m+\Delta\lambda/2, T)}{\sqrt{2}} e^{-2\pi x\kappa/\lambda_0}(\cos\frac{-2\pi xn}{\lambda_0} + i\sin\frac{-2\pi xn}{\lambda_0}) \ . \quad \text{(B.1)}$$

The complex conjuagete of Equation B.1 is simply

$$E^*_{in,y}(x,\lambda,\Delta\lambda,T) = \frac{\tilde{E}_t(\Delta\lambda, T)}{\sqrt{2}} e^{-2\pi x\kappa/\lambda_0}(\cos\frac{-2\pi xn}{\lambda_0} - i\sin\frac{-2\pi xn}{\lambda_0}) \ . \quad \text{(B.2)}$$

Equation 3.50 can be rewritten as

$$E_{y,r}(x,\lambda,\Delta\lambda,T) = \frac{-|E_t(\Delta\lambda,T)|}{\sqrt{2}} [e^{2\pi x(\kappa)/\lambda_0}(\cos\frac{2\pi xn}{\lambda_0} + i\sin\frac{2\pi xn}{\lambda_0}))][e^{-4\pi\ell(\kappa)/\lambda_0}(\cos\frac{-4\pi\ell n}{\lambda_0} + i\sin\frac{-4\pi\ell n}{\lambda_0})] \ . \quad \text{(B.3)}$$

The complex conjuagete of Equation B.4 is simply

$$E_{y,r}(x,\lambda,\Delta\lambda/,T) = \frac{-|E_t(\Delta\lambda,T)|}{\sqrt{2}}$$
$$[e^{2\pi x(\kappa)/\lambda_0}(\cos\frac{2\pi xn}{\lambda_0} - i\sin\frac{2\pi xn}{\lambda_0}))][e^{-4\pi\ell(\kappa)/\lambda_0}(\cos\frac{-4\pi\ell n}{\lambda_0} - i\sin\frac{-4\pi\ell n}{\lambda_0})] \ . \quad \text{(B.4)}$$

Now using Equation 3.47, the heat generation for the incident-reflecting case is obtained. Simplifying this equation using *Mathematica*, one gets Equation 3.51.

Appendix C

Monte Carlo Ray Tace Method FORTRAN 77 Code

```
*                                                                      *
      PROGRAM MONTECARLO

      IMPLICIT NONE

      INTEGER i, j, k, numrays, jmax, kmax, seed1, seed2
      PARAMETER(numrays = 10000000, jmax = 10, kmax = 1)
      REAL pi, kappa, kk, re, lambda, mu,  c0, Y, ranmar, sa, N,
     + NR, sum
      DIMENSION Y(jmax), sa(numrays), N(jmax,kmax), NR(kmax)
      EXTERNAL ranmar
```

```
C  Control Volume Discretization
Y(1)=1E-6
Y(2)=2E-6
Y(3)=3E-6
Y(4)=4E-6
Y(5)=5E-6
Y(6)=6E-6
Y(7)=7E-6
Y(8)=8E-6
Y(9)=9E-6
Y(10)=10E-6

OPEN(1,FILE='jose.txt')

C Parameters

pi=ACOS(-1.) ! Definition of the number pi
re=0.00025 ! Electrical Resistivity of the Absorber Layer in Ohm-m
lambda=50.5E-6
mu=pi*4E-7
c0=2.997E8 ! Speed of light in vacuum
kk=sqrt(lambda*mu*c0/(4*pi*re))
WRITE(1,*) kk
```

```
C  Calculate the Spectral Absorption Coefficient and Spectral Scattering Coefficient

kappa=4*pi*kk/lambda


C Setting the number of rays fired within wavelength band k to zero.
C Setting the number of rays fired and hit control volume j to zero.

DO 6 j=1,jmax
DO 7 k=1,kmax
NR(k)=0
N(j,k)=0

7  CONTINUE
6 CONTINUE


C  Pseudo-Random Number Generator

seed1=1802
seed2=9373
CALL rmarin(seed1,seed2)


C Launch Rays
```

```
DO 50 i=1,numrays
DO 100 k=1,kmax



C  Compute the free path of the energy bundel B4 it be absorbed


sa(i)=-1/kappa*LOG(1-ranmar())


C Launching rays from the surface
j=1


C Absorption Algorithm
DO WHILE (j .le. 10)


if (sa(i) .gt. Y(10)) then
C if (j .eq. 10) then
C write(*,*)'sa is', sa(i)
C end if
if (sa(i) .lt. Y(10)+Y(j)) then
N(11-j,k)=N(11-j,k)+1
NR(k)=NR(k)+1
j=11


else
```

```
j=j+1
end if
else
if (sa(i) .lt. Y(j)) then
N(j,k)=N(j,k)+1
NR(k)=NR(k)+1
j=11
else
j=j+1
end if
end if

if (sa(i) .gt. 2*Y(10)) then
if (j .eq. 10) then
write(*,*)'ERROR. Ray has not been absorbed!'
write(*,*)'Ray has reflected and hit air/absorber'
write(*,*)'interface.'
write(*,*)'Ray could have rebounded back in absorber'
write(*,*)'or gone into air'
write(*,*)
end if
end if

END DO
```

```
100 CONTINUE
50 CONTINUE

WRITE(*,*)'Wavelength is',lambda,' microns.'
WRITE(*,*)'Total Number of Rays Launched in Wavelength k is',numrays
WRITE(*,*)'Total Number of Rays absorbed Wavelength k is',NR(1)
WRITE(*,*)
WRITE(*,*)'Number of rays absorbed by bin 1 is', N(1,1)
WRITE(*,*)'Number of rays absorbed by bin 2 is', N(2,1)
WRITE(*,*)'Number of rays absorbed by bin 3 is', N(3,1)
WRITE(*,*)'Number of rays absorbed by bin 4 is', N(4,1)
WRITE(*,*)'Number of rays absorbed by bin 5 is', N(5,1)
WRITE(*,*)'Number of rays absorbed by bin 6 is', N(6,1)
WRITE(*,*)'Number of rays absorbed by bin 7 is', N(7,1)
WRITE(*,*)'Number of rays absorbed by bin 8 is', N(8,1)
WRITE(*,*)'Number of rays absorbed by bin 9 is', N(9,1)
WRITE(*,*)'Number of rays absorbed by bin 10 is', N(10,1)
WRITE(*,*)
WRITE(*,*)
WRITE(*,*)'Dijk in bin 1 is',N(1,1)/NR(1)
WRITE(*,*)'Dijk in bin 2 is',N(2,1)/NR(1)
WRITE(*,*)'Dijk in bin 3 is',N(3,1)/NR(1)
WRITE(*,*)'Dijk in bin 4 is',N(4,1)/NR(1)
WRITE(*,*)'Dijk in bin 5 is',N(5,1)/NR(1)
WRITE(*,*)'Dijk in bin 6 is',N(6,1)/NR(1)
```

```
WRITE(*,*)'Dijk in bin 7 is',N(7,1)/NR(1)
WRITE(*,*)'Dijk in bin 8 is',N(8,1)/NR(1)
WRITE(*,*)'Dijk in bin 9 is',N(9,1)/NR(1)
WRITE(*,*)'Dijk in bin 10 is',N(10,1)/NR(1)
sum=N(1,1)+N(2,1)+N(3,1)+N(4,1)+N(5,1)+N(6,1)+N(7,1)+N(8,1)+N(9,1)+N(10,1)
WRITE(*,*)
WRITE(*,*)'Sum of Dijs',sum/NR(1)
STOP
END  PROGRAM MONTECARLO
```

```
*                                                                    *
**********************************************************************
*   Subroutine that generates Random Numbers                         *
**********************************************************************
*                                                                    *
subroutine rmarin(ij, kl)
C
C This is the initialization routine for the random number
c generator ranmar().
c NOTE: The seed variables can have values between:
C    0 <= IJ <= 31328
C    0 <= KL <= 30081
```

```
C The random number sequences created by these two seeds are of
C sufficient length to complete an entire calculation with. For
c example, if sveral different groups are working on different
c parts of the same calculation, each group could be assigned its
c own IJ seed. This would leave each group with 30000 choices for
c the second seed. That is to say, this random number generator can
c create 900 million different subsequences -- with each
c subsequence having a length of approximately 10^30.
C
C Use IJ = 1802 & KL = 9373 to test the random number generator.
c The subroutine ranmar should be used to generate 20000 random
c numbers.  Then display the next six random numbers generated
c multiplied by 4096*4096.  If the random number generator is
c working properly, the random numbers should be:
C           6533892.0  14220222.0  7275067.0
C           6172232.0  8354498.0   10633180.0
c
c      implicit real*8 (a-h, o-z)
      real*8 u(97), c, cd, cm, s, t
      integer ii, i, j, ij, jj, k, kl, l, m, i97, j97
      logical test
      common /raset1/ u, c, cd, cm, i97, j97, test
      test = .false.
c
      if( IJ .lt. 0  .or.  IJ .gt. 31328  .or.
```

```
S    KL .lt. 0  .or.  KL .gt. 30081 ) then
      write (*, *) ' The first random number seed must have a'
      write (*, *) ' value between 0 and 31328.'
      write (*, *)
      write (*, *) ' The second seed must have a value between 0'
      write (*, *) ' and 30081.'
      write (*, *) 'Stopping...'
      stop
    endif
c
    i = mod(IJ/177, 177) + 2
    j = mod(IJ    , 177) + 2
    k = mod(KL/169, 178) + 1
    l = mod(kl,     169)
c
    do 2 ii = 1, 97
      s = 0.0
      t = 0.5
      do 3 jj = 1, 24
        m = mod(mod(i*j, 179)*k, 179)
        i = j
        j = k
        k = m
        l = mod(53*l+1, 169)
        if (mod(l*m, 64) .ge. 32) then
```

```
               s = s + t
            endif
            t = 0.5 * t
 3  continue
        u(ii) = s
 2 continue
c
      c = 362436.0 / 16777216.0
      cd = 7654321.0 / 16777216.0
      cm = 16777213.0 /16777216.0
c
      i97 = 97
      j97 = 33
c
      test = .true.
c
      return
      end



      real*8 function ranmar()
c
c This is the random number generator proposed by George Marsaglia
c in Florida State University Report: FSU-SCRI-87-50
c
```

```
c      implicit real*8 (a-h, o-z)
       real*8 u(97), uni, c, cd, cm
       integer i97, j97
       logical test
       common /raset1/ u, c, cd, cm, i97, j97, test
c
       if(.not.test) then
          write (*, *)
          write (*, *) 'ranmar error #1: must call the'
          write (*, *) 'initialization routine rmarin before'
          write (*, *) 'calling ranmar.'
          write (*, *) 'Stopping...'
          stop
       endif
c
       uni = u(i97) - u(j97)
       if( uni .lt. 0.0 ) uni = uni + 1.0
       u(i97) = uni
       i97 = i97 - 1
       if(i97 .eq. 0) i97 = 97
       j97 = j97 - 1
       if(j97 .eq. 0) j97 = 97
       c = c - cd
       if( c .lt. 0.0 ) c = c + cm
       uni = uni - c
```

```
      if( uni .lt. 0.0 ) uni = uni + 1.0
c
      ranmar = uni
c
      return
      end
```

Vita

José Dobarco-Otero was born on September 19, 1977, in Pontevedra, Spain. He moved to the United States in July of 1988. He attended Mount Vernon High School, where he graduated as the Valedictorian of his class in June of 1995. That August he enrolled at Virginia Polytechnic Institute and State University in Blacksburg, Virginia. In May of 1999 he graduated (Magna Cum Laude) with a Bachelor of Science degree in Mechanical Engineering. He then pursued a Master of Science degree at the same institution, concentrating on heat transfer.